

Check for updates

# Plaque-Targeted Delivery of Fluoride-Free MXene Nanozyme for Alleviating Atherosclerosis via Sonocatalytic Therapy

Qianqian Bai, Xinyue Lao, Sin-Yi Pang, Yifei Zhao, Yuan Liu, Xiao Yu Tian, and Jianhua Hao\*

Atherosclerosis is an oxidative stress-induced chronic inflammatory condition underpinning the progression of cardiovascular diseases (CVDs), ultimately resulting in leading mortality rate globally. Ultrasound (US)-triggered catalysis offers localized treatment for deep-seated plaques effectively and safely, with demand for targeted delivery and anti-inflammatory properties of sonosensitizers. 2D MXene-based nanomedicine is garnering attention because of their intriguing catalytic properties of scavenging excessive reactive oxygen species (ROS), yet MXene-assisted sonocatalytic therapy (SCT) for treating CVDs remains scarce. Here, this study reports a dual enzymemimicking and US-responsive MXene termed Nb2C-Pt@HA-PEG for alleviating atherosclerosis. US irradiation enhances the capability of Nb2C-Pt@HA-PEG nanozymes in eliminating broad-spectrum ROS and resolving vascular inflammation. Besides, actively targeting lesional macrophages improves their systemic delivery to plaque and further boosts anti-atherosclerotic efficacy, contributing to ≈30% plaque size reduction and a more stabilized plaque phenotype. Notably, etching without hydrofluoric acid renders this nanozyme highly biocompatible. In long-term biosafety studies, Nb<sub>2</sub>C-Pt@HA-PEG is pronouncedly cleared from major organs and no severe changes of liver and kidney functions are observed. Consequently, this work demonstrates that Nb<sub>2</sub>C-Pt@HA-PEG-mediated SCT effectively ameliorates advanced atherosclerosis without inducing severe cytotoxicity, offering promising translational potential of MXene-based nanomedicine. Besides, it broadens application prospects of MXenes to the biomedical field of treating CVDs.

1. Introduction

Atherosclerosis is a chronic inflammatory condition underpinning the progression of CVDs, resulting in the leading mortality

rate globally.[1] Reactive oxygen species (ROS) plays a fundamental role in regulating vascular redox homeostasis whereas excessive ROS induced by cardiovascular risk factors (e.g., hypertension, hyperlipidemia and diabetes) increases oxidative stress from various sources including nicotinamide adenine dinucleotide phosphate (NADPH) oxidases (NOX) and mitochondrial electron transport chain.[2] Oxidative stress is a critical contributor to early stage of endothelial dysfunction, which scavenges nitric oxide (NO) therefore reduces NO bioavailability.[3] Furthermore, sustained ROS overproduction induces oxidative modifications of low density lipoproteins (LDL) to become oxidized LDL (oxLDL), which further impairs endothelial function, triggers inflammation and macrophage polarization and initiates atherogenesis.[4] Increased oxLDL also facilitates the accumulation of lipid-laden macrophages (foam cells), which can generate more ROS when forming atherosclerotic plaque.[5] Thus, high levels of ROS in the vascular microenvironment is a characteristic feature of advanced atherosclerotic plaque. [6]

Based on the critical contribution of ROS during atherogenesis and especially ROS-induced intraplaque inflammation, recent

studies attempted to target ROS as a potential intervention. Nanozymes are catalytic nanomaterials exhibiting intrinsic antioxidative properties and mimic natural enzymes to eliminate ROS.<sup>[7]</sup> To date, several nanomaterials have been employed

Q. Bai, X. Lao, S.-Y. Pang, Y. Zhao, Y. Liu, J. Hao Department of Applied Physics The Hong Kong Polytechnic University Hong Kong 999077, P. R. China E-mail: jh.hao@polyu.edu.hk

The ORCID identification number(s) for the author(s) of this article can be found under https://doi.org/10.1002/adma.202420189

© 2025 The Author(s). Advanced Materials published by Wiley-VCH GmbH. This is an open access article under the terms of the Creative Commons Attribution-NonCommercial-NoDerivs License, which permits use and distribution in any medium, provided the original work is properly cited, the use is non-commercial and no modifications or adaptations are made.

DOI: 10.1002/adma.202420189

X. Y. Tian

School of Biomedical Sciences The Chinese University of Hong Kong Hong Kong 999077, P. R. China

J. Had

Department of Biomedical Engineering The Hong Kong Polytechnic University Hong Kong 999077, P. R. China

J. Hao

Research Centre for Nanoscience and Nanotechnology The Hong Kong Polytechnic University Hong Kong 999077, P. R. China



ADVANCED MATERIALS

www.advmat.de

as nanozymes for anti-atherosclerosis efficacy, including black phosphorus nanosheets, hydrogen-intercalated palladium, Prussian Blue and ceria. [8] Furthermore, US has been proved to improve catalytic properties of nanozyme for scavenging ROS. [9] Sonocatalytic therapy (SCT) leverages US-responsive catalysts to regulate ROS by initiating various redox catalytic reactions for treating deep-seated diseases. [10] Therefore, SCT is another prospective treatment for alleviating atherosclerosis as local tissue penetration of US is up to  $\approx 10$  cm. [10b]

Although SCT owns the merits of high penetration depth and tunable treatment area, providing a suitable sonosensitizer for achieving therapeutic effects safely and efficiently remains challenging. MXenes, a family of 2D atomically thin nanosheets, are emerging inorganic nanoplatforms for biomedical applications attributing to their high planar surface area with abundant anchoring sites for elaborately engineering.[11] However, conventional hydrofluoric acid (HF)-mediated MXene synthesis historically limited practical clinical translation due to residual fluoride toxicity.[12] Our recently developed fluoride-free routine has circumvented this biosafety bottleneck, unleashing their untapped biomedical potential.<sup>[13]</sup> Noble metal- decorated MXenes have been demonstrated to act as nanozymes with amplified enzymelike antioxidative activities.[14] Additionally, introduction of noble metal allows MXenes serving as sonosensitizers through promoting the separation and suppressing the recombination of electron-hole pairs.[15] Overall, noble metal-deposited MXenebased nanozymes hold promising potential as sonosensitizer for SCT.

In this work, we present a fluoride-free biocompatible nanozyme termed as Nb2C-Pt@HA-PEG with US-augmented catalytic therapy for treating advanced atherosclerosis, overcoming aforementioned obstacles (Scheme 1). Herein, the noble metal platinum nanoparticles (PtNPs)-deposited Nb<sub>2</sub>C MXene serving as catalase (CAT)/superoxide dismutase (SOD)mimicking nanostructure exhibits exceptional broad-spectrum ROS-scavenging properties under US irradiation. Attaching hyaluronic acid (HA) endows this nanostructure with promoted delivery to atherosclerotic plaque by targeting CD44 receptors overexpressed on inflammatory macrophages and endothelial cells (ECs). To maintain the stability and biocompatibility for further preclinical studies, poly(ethylene glycol)2000 (PEG) was employed to achieve PEGylation on the Nb<sub>2</sub>C nanosheets by electrostatic adsorption. Specifically, the introduction of PtNPs to the surface of Nb<sub>2</sub>C confers a profound structural distortion through surficial interaction, and the resultant reduction in symmetry leads to enhanced generation of electrons and holes under US irradiation. Density functional theory (DFT) calculations demonstrate a significant electron transfer between PtNPs and Nb<sub>2</sub>C, which is beneficial to augment the enzyme-like activities. In addition, the PtNPs on the surface of Nb<sub>2</sub>C further facilitates electron transfer, ultimately enhancing the separation of electrons and holes. In vitro studies confirm that these rationally engineered Nb<sub>2</sub>C-Pt@HA-PEG nanozymes with promoted accumulation in the polarized macrophages scavenge diverse ROS and perform intrinsic antioxidative properties to dampen inflammatory responses related to atherogenesis. Upon US irradiation, Nb<sub>2</sub>C-Pt@HA-PEG-mediated SCT exhibits notably superior antioxidative and anti-inflammatory effects with augmented ROS elimination and inflammatory resolution. In vivo studies demonstrate that Nb<sub>2</sub>C-Pt@HA-PEG nanozymes selectively target atherosclerotic plaques upon an intravenous (i.v.) injection, with a  $\approx$ 3fold higher accumulation than that of Nb<sub>2</sub>C-Pt@PEG counterparts. Nb<sub>2</sub>C-Pt@HA-PEG-mediated SCT exerts an outstanding anti-atherosclerosis efficacy by regulating intraplaque redox homeostasis and inhibiting macrophage infiltration, contributing to  $\approx$ 30% lesional shrinkage, a thicker fibrous cap, and  $\approx$ 50% smaller necrotic core area. RNA-sequencing analysis further elucidates that the underlying molecular mechanisms driving these therapeutic effects are resolving inflammatory responses, promoting efferocytosis, inhibiting lipid uptake and maintaining redox homeostasis within the vascular microenvironment. Repeated i.v. administrations of this fluoride-free nanoplatform do not induce severe cytotoxicity, as evidenced by pronounced clearance from liver 4 weeks after full treatment and no significant change in the hepatic and renal functions and morphology of major internal organs.

#### 2. Results and Discussion

#### 2.1. Synthesis and Characterization of Nb<sub>2</sub>C MXenes

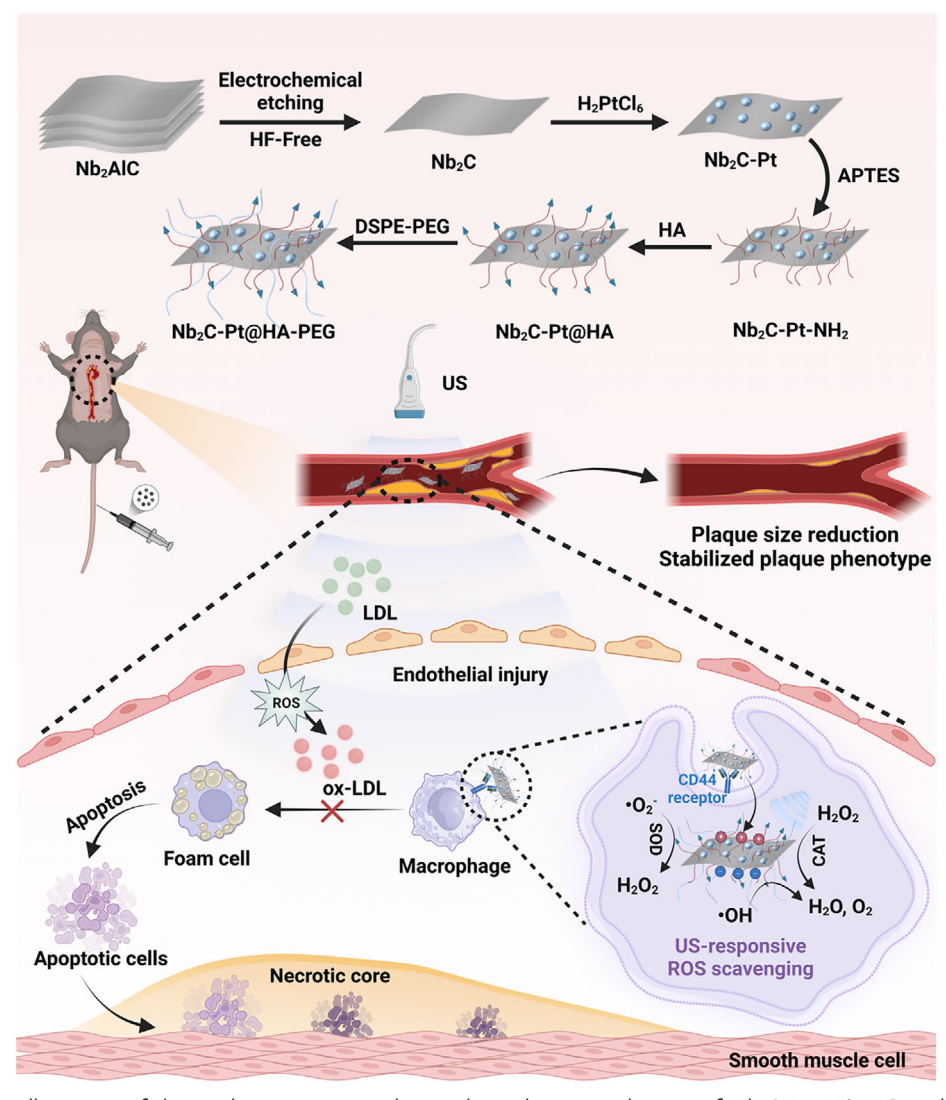
The 2D fluoride-free Nb<sub>2</sub>C MXenes were synthesized through an innovative electrochemical method based on our previous research.[13a] The schematic diagram of the crystallization of Pt-NPs on Nb<sub>2</sub>C MXenes and following modification with HA and PEGylation are illustrated in Figure 1A. In a typical synthesis process, the few-layer pristine Nb<sub>2</sub>C MXenes suspension was sonicated for 1 h to obtain MXenes, which were subsequently reacted with H<sub>2</sub>PtCl<sub>6</sub> and sodium citrate aqueous solution to fabricate Nb<sub>2</sub>C-Pt. The Nb<sub>2</sub>C-Pt MXenes were functionalized with amine group before conjugated with HA (Nb<sub>2</sub>C-Pt@HA) and finally encapsulated with DSPE-PEG (Nb<sub>2</sub>C-Pt@HA-PEG). The scanning electron microscopy (SEM) image reveals the pristine Nb<sub>2</sub>C MXene exhibiting few-layered nanosheet structure (Figure 1B). The element mapping confirmed that Nb and Pt are evenly distributed throughout Nb<sub>2</sub>C-Pt nanosheets (Figure S1A, Supporting Information). The morphology of Nb2C and Nb2C-Pt was further examined with transmission electron microscopy (TEM). The TEM images show the prepared pristine Nb<sub>2</sub>C with an average thickness of  $\approx 0.63$  nm (Figure 1C; Figure S1B, Supporting Information) and Nb<sub>2</sub>C-Pt possesses consistent nanosheet morphology with pristine Nb₂C, with PtNP (≈5 nm) distributed on the surface (Figure 1D).

To further investigate the chemical composition of the obtained Nb<sub>2</sub>C-Pt MXenes, X-ray diffraction (XRD) and X-ray photoelectron spectroscopy (XPS) were performed (Figure 1E–G). XRD analysis indicates the elimination of characteristic peaks of Nb<sub>2</sub>AlC in both Nb<sub>2</sub>C and Nb<sub>2</sub>C-Pt samples while Nb<sub>2</sub>C-Pt nanosheets display distinctive peaks for PtNP from pristine Nb<sub>2</sub>C, closely aligning with the standard peaks for Pt (111) and (200) (Figure 1E).<sup>[16]</sup> In addition, while the pristine Nb<sub>2</sub>C crystal structure guides the Pt deposition process, the characteristic peaks of Nb<sub>2</sub>C (100) and (103) remain unchanged after Pt decoration, indicating preservation of the substrate's structural integrity. Only additional peaks corresponding to metallic Pt are observed, confirming successful deposition without compromising the underlying MXene structure. The survey XPS spectrum further confirms the growth of PtNP on the Nb<sub>2</sub>C

15214095, 0, Downloaded from https://advanced.onlinelibrary

wiley.com/doi/10.1002/adma.202420189 by HONG KONG POLYTECHNIC UNIVERSITY HU NG HOM, Wiley Online Library on [2609/2025]. See the Terms

and-conditions) on Wiley Online Library for rules of use; OA articles are governed by the applicable Creative Commons



Scheme 1. Schematic illustration of the synthesis strategy and anti-atherosclerotic mechanism of  $Nb_2C$ -Pt@HA-PEG-mediated SCT. This work started with an evaluation of the ROS-scavenging capability of  $Nb_2C$ -Pt@HA-PEG nanozymes. The targeted delivery of  $Nb_2C$ -Pt@HA-PEG and enzyme-mimicking, ROS-eliminating and anti-inflammatory capability of  $Nb_2C$ -Pt@HA-PEG-mediated SCT were then investigated using RAW 264.7 macrophages in vitro. The pharmacokinetics and biodistribution (especially within atherosclerotic lesion) of  $Nb_2C$ -Pt@HA-PEG were assessed in a plaque-bearing  $ApoE^{-/-}$  mouse model. Notably, we then evaluated the anti-atherosclerotic efficacy, plaque destabilization and rupture inhibition effect, and the therapeutic mechanism of  $Nb_2C$ -Pt@HA-PEG-mediated SCT in vivo. Additionally, RNA-sequencing was employed to elucidate the molecular mechanisms involved in macrophages treated with  $Nb_2C$ -Pt@HA-PEG-mediated SCT. Finally, the long-term safety profile of  $Nb_2C$ -Pt@HA-PEG-mediated SCT was evaluated in vivo.

substrate (Figure 1F). Figure 1G presents the Pt  $4d_{5/2}$  XPS profile for Nb<sub>2</sub>AlC, Nb<sub>2</sub>C, and Nb<sub>2</sub>C-Pt, featuring a prominent doublet at 315.8 eV and 332.8 eV, corresponding to the Pt (II) and Pt (IV) chemical states indicative of species such as PtH<sub>x</sub>O<sub>y</sub>. Besides, the XPS spectrum reveals deconvoluted peaks, resulting in a broad peak at 335.4 eV, the characteristic of Pt<sup>0</sup> state. After confirming the successful crystallization of PtNP on the pristine Nb<sub>2</sub>C substrate, complementary XPS was performed to explore the synergistic interaction between Pt and Nb<sub>2</sub>C. The Pt 4f peaks (Figure S1C, Supporting Information,  $4f_{7/2}$  at 72.36 eV and  $4f_{5/2}$  at 75.25 eV) show a notable positive shift ( $\approx$ 1.1–1.2 eV) compared to typical metallic Pt<sup>0</sup> values, indicating strong metal-support interaction (SMSI) with Nb<sub>2</sub>C, while maintaining the

characteristic splitting of  $\approx\!2.9$  eV. Additionally, the presence of Pt 4d peaks (332.77, 335.42, 319.06, and 315.8 eV) further confirms the electronic state of Pt and its interaction with the substrate (Figure 1G). Taken together, these combined results indicate both electronic interaction through charge transfer and structural integration between Pt and Nb<sub>2</sub>C, suggesting clear SMSI effects.

Next, the synthesis of Nb<sub>2</sub>C-Pt@HA was obtained via EDC/NHS chemistry between amine-modified Nb<sub>2</sub>C-Pt (Nb<sub>2</sub>C-Pt-NH<sub>2</sub>) and HA. The dynamic light scattering (DLS) was employed to verify the zeta potentials ( $\zeta$ -potentials) after surface modification of Nb<sub>2</sub>C. The  $\zeta$ -potential of Nb<sub>2</sub>C-Pt appeared to shift from –34.7 mV to +20.3 mV (Nb<sub>2</sub>C-Pt-NH<sub>2</sub>) and –27.8 mV (Nb<sub>2</sub>C-Pt@HA), respectively, suggesting successful modification

wiley.com/doi/10.1002/adma.202420189 by HONG KONG POLYTECHNIC UNIVERSITY HU NG HOM, Wiley Online Library on [26/09/2025]. See the Terms

conditions) on Wiley Online Library for rules of use; OA articles are governed by the applicable Creative Commons

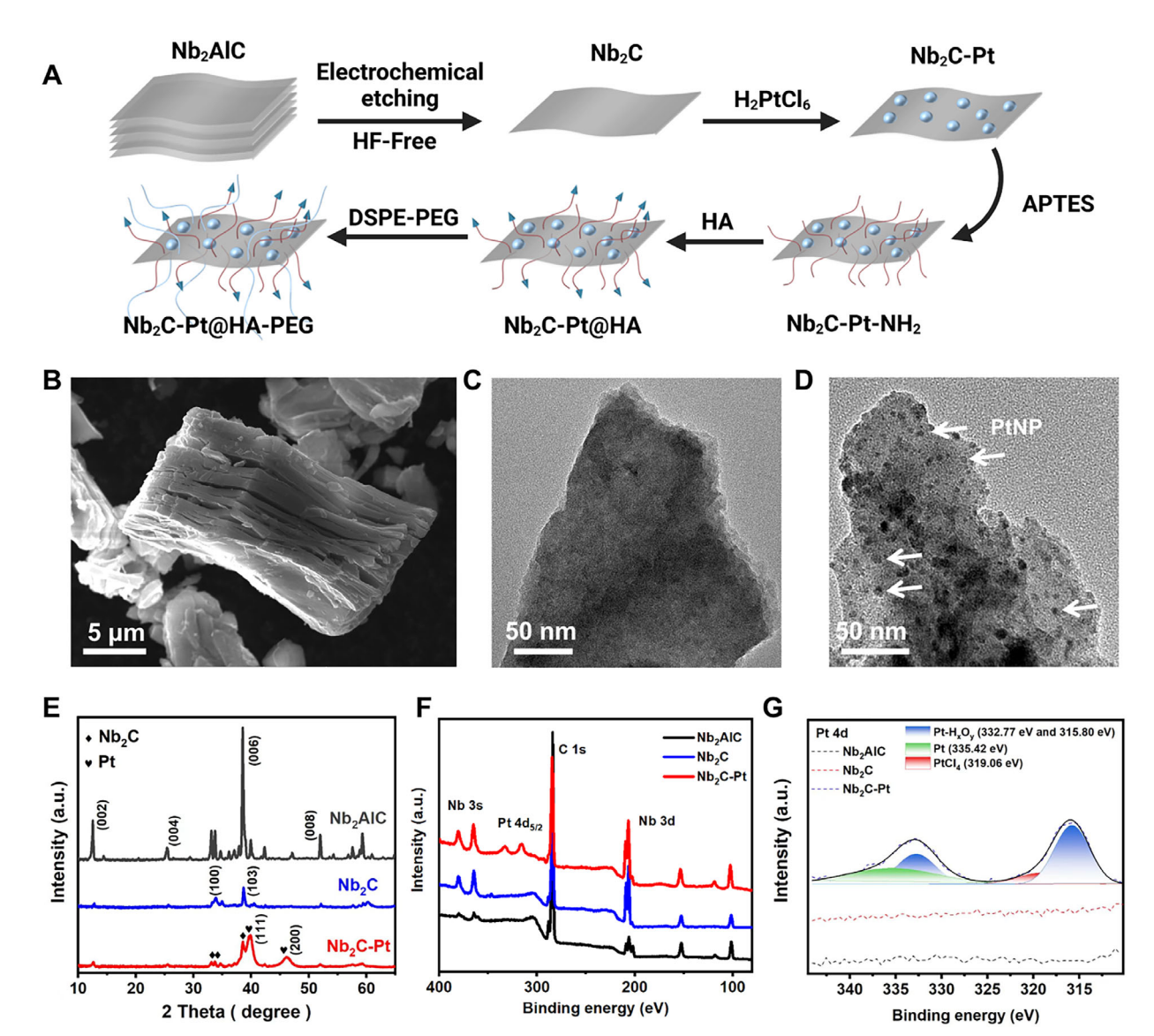


Figure 1. Characterization of Nb<sub>2</sub>C MXenes. A) Schematic diagram of synthesis procedure of Nb<sub>2</sub>C-Pt@HA-PEG. B) Representative SEM images of multilayer pristine Nb<sub>2</sub>C. Representative TEM images of single-layer C) pristine Nb<sub>2</sub>C and D) Nb<sub>2</sub>C-Pt. E) XRD patterns of Nb<sub>2</sub>AlC, Nb<sub>2</sub>C and Nb<sub>2</sub>C-Pt nanosheets. The curves were normalized for comparison. F) XPS survey and G) high-resolution XPS of Pt 4d region in Nb<sub>2</sub>AlC, Nb<sub>2</sub>C and Nb<sub>2</sub>C-Pt nanosheets.

of amine-group and HA (Figure S1D, Supporting Information). To improve the biocompatibility of Nb<sub>2</sub>C-Pt@HA for further biological applications, we decorated Nb<sub>2</sub>C MXenes with PEG, a NP stabilizing agent in cardiovascular nanomedicine delivery applications. Nb<sub>2</sub>C-Pt@HA-PEG was synthesized by sonication with Nb<sub>2</sub>C-Pt@HA and DSPE-PEG<sub>2000</sub> solution. As shown in Figure S1D (Supporting Information), the  $\zeta$ -potential of Nb<sub>2</sub>C-Pt@HA-PEG is -28.3 mV.

# 2.2. The ROS-Scavenging Performance of Nb₂C-Pt@HA-PEG Nanozymes

Overproduction of ROS in the microenvironment of atherosclerotic plaque persistently increases cellular oxidative stress and

further induces chronic inflammation and vascular damage, playing a pivotal role in the pathogenesis of atherosclerosis.<sup>[2-4]</sup> Therefore, we started with examining whether Nb<sub>2</sub>C-Pt@HA-PEG nanosheets can impair the ROS generation. First, the general ROS-scavenging performance of Nb<sub>2</sub>C-Pt@HA-PEG nanosheets was tested by using the typical 2,2'-Azino-bis-3-ethylbenzthiazoline-6-sulfonic acid (ABTS) assay. The antioxidant capacity was presented by Trolox-equivalent antioxidant capacity (TEAC), an analogue of vitamin E featuring similar antioxidant properties to vitamin.<sup>[19]</sup> The results showed that Nb<sub>2</sub>C-Pt and Nb<sub>2</sub>C-Pt@HA-PEG nanosheets shared similarly stronger TEAC than pristine Nb<sub>2</sub>C with or without US irradiation, indicating that Pt-modification renders Nb<sub>2</sub>C-Pt and Nb<sub>2</sub>C-Pt@HA-PEG nanosheets with more effective ROS clearance capability (Figure 2A).<sup>[20]</sup> Furthermore, to assess specific enzyme-like

www.advmat.de

15214095, 0, Downloaded from https://advanced.onlinelibrary.wiley.com/doi/10.1002/adma.202420189 by HONG KONG POLYTECHNIC UNIVERSITY HU NG HOM, Wiley Online Library on [26.09/2025]. See the Terms

conditions) on Wiley Online Library for rules of use; OA articles are governed by the applicable Creative Commons I

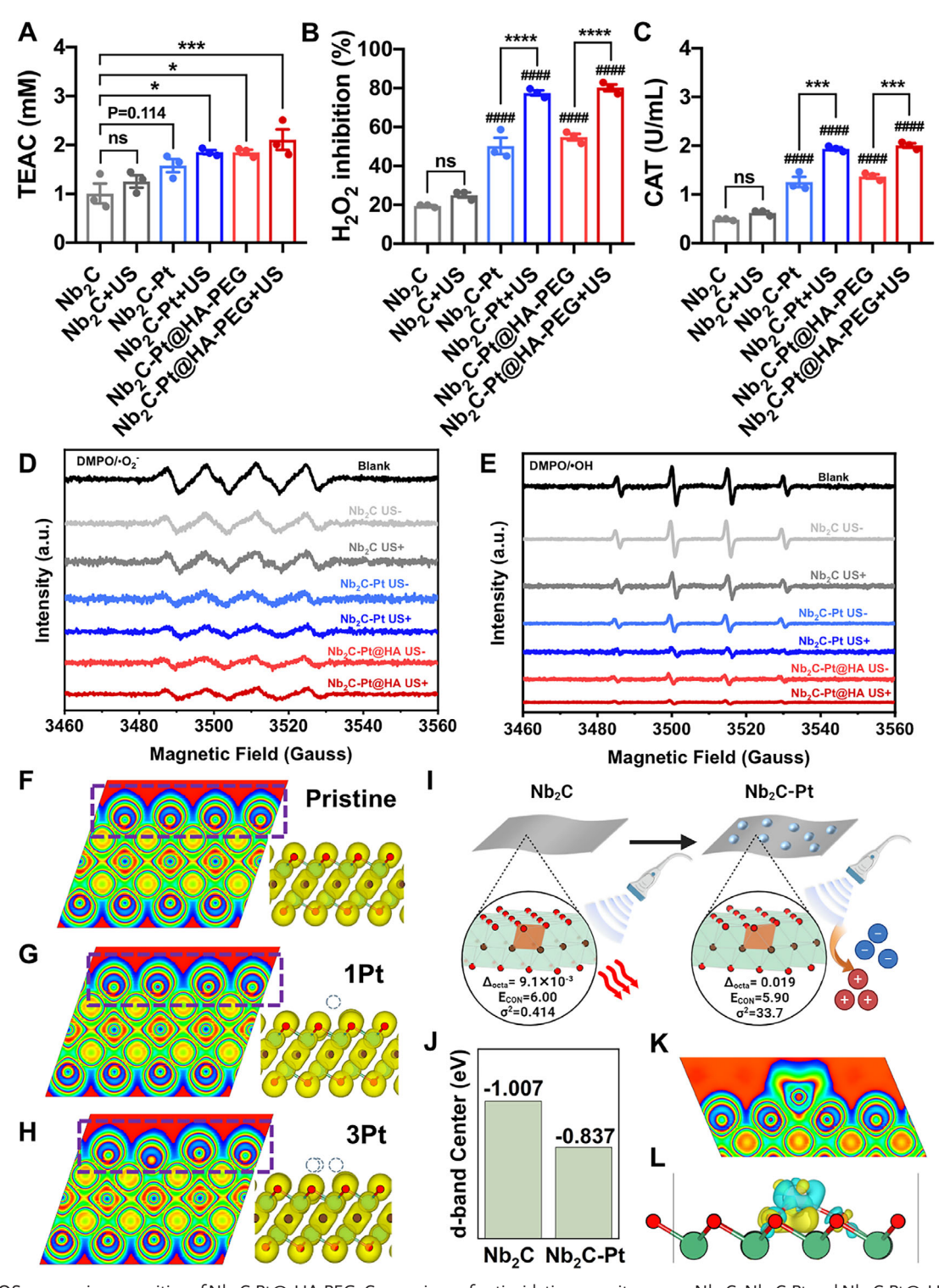


Figure 2. ROS-scavenging capacities of Nb<sub>2</sub>C-Pt@-HA-PEG. Comparison of antioxidative capacity among Nb<sub>2</sub>C, Nb<sub>2</sub>C-Pt and Nb<sub>2</sub>C-Pt@-HA-PEG under US irradiation or non-US conditions by A) ABTS method and B,C) CAT assay (n = 3). All the data are presented as mean  $\pm$  SEM. Statistical significance was calculated by one-way ANOVA with Tukey's test for post hoc analysis. ns: not significant (P > 0.05), \*P<0.05, \*\*\*P<0.001, \*\*\*\*P<0.0001, \*\*\*\*P<0.0001, \*\*\*\*P<0.0001. ESR spectra of D)  $\bullet$ O<sub>2</sub> and E)  $\bullet$ OH trapped by DMPO with pristine Nb<sub>2</sub>C, Nb<sub>2</sub>C-Pt or Nb<sub>2</sub>C-Pt@-HA-PEG or their US-irradiated counterparts. 2D slice and 3D ELF diagram of F) pristine Nb<sub>2</sub>C MXene, G) Nb<sub>2</sub>C adsorbed by 1 Pt atom and H) Nb<sub>2</sub>C adsorbed by a Pt cluster. The blue and red regions correspond to electron delocalization and localization, respectively. I) Schematic illustration of the Pt-adsorption-induced local symmetry breaking of Nb<sub>2</sub>C, leading to the emergent US-responsive properties. J) Calculated d-band center of Nb<sub>2</sub>C and Nb<sub>2</sub>C-Pt. K) ELF featuring the interfaces between Nb<sub>2</sub>C and adsorbed Pt. L) CDD diagram of interfaces within Nb<sub>2</sub>C-Pt, the yellow and cyan areas correspond to electron accumulation and depletion, respectively.



ADVANCED MATERIALS

www.advmat.de

catalytic properties of Nb2C-Pt@HA-PEG nanosheets as sonosensitizers, three representative ROS, including hydrogen peroxide ( $H_2O_2$ ), superoxide anion ( $\bullet O_2^-$ ) and hydroxyl radical (•OH) were tested for comparing the ROS-scavenging activities among pristine Nb<sub>2</sub>C, Nb<sub>2</sub>C-Pt and Nb<sub>2</sub>C-Pt@HA-PEG nanosheets, respectively. Initially, we investigated the CAT-like property of Nb<sub>2</sub>C MXenes. CAT, an enzyme in the vascular wall, catalyzes the decomposition of H<sub>2</sub>O<sub>2</sub>, acting as antioxidant defense system to reduce intraplaque ROS burden.[2a] Nearly 50.2% and 54.8% of H2O2 were scavenged by Nb2C-Pt and Nb<sub>2</sub>C-Pt@HA-PEG MXenes, respectively, which had ≈30% improvement compared to their pristine Nb<sub>2</sub>C counterparts (Figure 2B). Additionally, both Nb<sub>2</sub>C-Pt+US group (77.5%) and Nb<sub>2</sub>C-Pt@HA-PEG+US (80.2%) group revealed a ≈25% increase in H<sub>2</sub>O<sub>2</sub> inhibition rate than Nb<sub>2</sub>C-Pt group (50.2%) and Nb<sub>2</sub>C-Pt@HA-PEG (54.8%), accompanied by no significant difference was found between pristine Nb<sub>2</sub>C group and pristine Nb<sub>2</sub>C+US group. Therefore, these data not only suggested that Pt-deposited Nb<sub>2</sub>C MXenes performed higher CAT-like enzymatic activities than pristine Nb2C, but also demonstrated that the resultant boosted ROS-scavenging capabilities under US treatment derived from their US-responsiveness (Figure 2C). SOD is another key antioxidant enzyme in regulating redox homeostasis by catalyzing the dismutation reaction of  $\bullet O_2^-$  radicals into biologically less harmful H2O2 and O2. [2b] Next, the SOD-like activities of Nb<sub>2</sub>C MXenes were evaluated by electron spin resonance (ESR) using 5,5-Dimethyl-1-Pyrroline-N-Oxide (DMPO) as spin trapping agent. •O2- radicals were initially produced by catalysis of H2O2 under light for mimicking the intraplaque microenvironment with excessive ROS. The ESR intensities of  $\bullet O_2^-$  from Nb<sub>2</sub>C-Pt and Nb<sub>2</sub>C-Pt@HA-PEG groups were lower than Nb<sub>2</sub>C group with or without US irradiation, indicating the similarly superior SOD-like catalytic properties of both Pt-deposited nanosheets than pristine Nb2C in quenching  $\bullet$ O<sub>2</sub> radicals (Figure 2D). Finally, we investigated the capability of Nb<sub>2</sub>C MXenes to offset excessive •OH radicals, the most potent oxidizing and biologically damaging species inducing inflammation and tissue injury.[21] •OH radicals were generated by Fenton reaction between Fe<sup>2+</sup> and H<sub>2</sub>O<sub>2</sub>. Nb<sub>2</sub>C-Pt and Nb<sub>2</sub>C-Pt@HA-PEG diminished •OH radicals in the same manner as evidenced by similarly partial reduction in the ESR intensities of •OH (Figure 2E). However, pristine Nb<sub>2</sub>C group showed no obvious change from control group, demonstrating the inherent ROS-scavenging properties of Nb2C-Pt@HA-PEG nanozymes. Furthermore, there was significant decline in ESR intensities of •OH radicals after Nb2C-Pt-mediated or Nb2C-Pt@HA-PEG-mediated sonocatalytic treatment compared with sole nanozymes groups. Comparatively, no significant difference was detected between pristine Nb<sub>2</sub>C group and Nb<sub>2</sub>C+US group (Figure 2E). Collectively, these data suggested that both Nb<sub>2</sub>C-Pt and Nb<sub>2</sub>C-Pt@HA-PEG nanosheets not only solely acted as nanozymes in diminishing diverse free radicals formation, but also featured superior CAT-like and SOD-like antioxidant properties upon US irradiation.

Since both Nb<sub>2</sub>C-Pt and Nb<sub>2</sub>C-Pt@HA-PEG nanozymes possess better catalytic properties in eliminating ROS than pristine Nb<sub>2</sub>C nanosheets under US treatment, the significantly en-

hanced US-responsiveness can be explained by the emergence of piezoelectric properties upon PtNP functionalization.<sup>[22]</sup> Piezoelectricity originates from the absence of an inversion center in the material's structure, leading to off-centered negative and positive charges upon external force application. For lowdimensional materials such as MXenes, modifications through strain engineering, surface functionalization, or adsorption of single atoms/NPs can significantly alter their local structure, giving rise to emergent piezoelectricity or even ferroelectricity.<sup>[23]</sup> To elucidate the physical origins of enhanced US-responsive properties in PtNPs-functionalized Nb2C MXene, DFT simulations were carried out. The pristine Nb<sub>2</sub>C MXene structure was constructed based on the Nb2AlC structure with oxygen terminal groups, which is consistent with our previous report. [13b] The electron localization function (ELF) analysis of pristine Nb<sub>2</sub>C (Figure 2F) reveals perfectly symmetric electron configurations on both surfaces, as evidenced in both 2D and 3D representations. Here, Pt was omitted after geometry relaxation to focus on the symmetry variation of MXene imposed by Pt adsorption. Upon single Pt atom adsorption, the local structure of the MXene surface begins to deviate from its initial symmetric configuration due to surface interactions, similar to the effect imposed by terminal groups. [22,23c] As shown in Figure 2G, the ELF diagrams of MXene influenced by one Pt have already shown some noticeable changes. When a Pt cluster is introduced, more pronounced structural distortion is observed (Figure 2H). The impact of Pt adsorption on Nb<sub>2</sub>C local structure can be quantified through distortion indices of the local polyhedra. As shown in Figure 2I, the NbC<sub>3</sub>O<sub>3</sub> octahedra undergoes significant distortion upon Pt adsorption. In specific, the octahedral distortion index ( $\Delta_{oct}$ ) increase from  $9.1 \times 10^{-3}$  to 0.019, while the bond angle variation  $(\sigma^2)$  boosted from 0.414 to 33.7 deg<sup>2</sup>. These changes indicate a transformation from nearly perfect octahedra to distorted ones, resulting in a reduced effective coordination number ( $E_{CoN}$ ) from 6.00 to 5.90.<sup>[24]</sup> In contrast, the NbC<sub>3</sub>O<sub>3</sub> polyhedra on the opposite surface experience minimal structural changes, creating an asymmetric distortion pattern across the whole MXene lattice. This spatial variation in symmetry breaking can effectively induce piezoelectric properties in the PtNP-functionalized MXene structure, leading to enhanced response to US treatments.

Furthermore, metal atom or NP modification is known to enhance the catalytic activity of MXenes.[14a,25] In our system, Pt adsorption shifts the d-band center (Figure 2J) to a higher energy level (-0.837 eV) compared to the pristine one (-1.007 eV), indicating enhanced oxygen affinity during the ROS-scavenging process.<sup>[26]</sup> The ELF (Figure 2K) and charge density difference (CDD, Figure 2L) featuring the Pt-MXene interface analyses demonstrate pronounced electron transfer and strong electronic interactions between MXene and the adsorbed Pt, suggesting an efficient charge transfer from MXene to Pt. This enhanced electronic interaction may facilitate scavenging ROS through more effective charge transfer. While our simulations employed a simplified Pt-atom adsorption model to maintain computational efficiency, the effects of PtNPs adsorption are expected to be more pronounced in actual systems.





www.advmat.de

# 2.3. In Vitro Antioxidative and Anti-Inflammatory Performance of Nb<sub>2</sub>C-Pt@HA-PEG-Mediated SCT

We have demonstrated that the introduction of PtNP endowed Nb<sub>2</sub>C-Pt and Nb<sub>2</sub>C-Pt@HA-PEG with superior catalytic properties than pristine Nb<sub>2</sub>C MXene and US-responsiveness. Next, we investigated whether the modification of HA ligands improves the targeted delivery of Nb<sub>2</sub>C-Pt@HA-PEG nanosheets to inflammatory macrophages for further amplifying their antioxidative effects in vitro. Thus, we first evaluated the cytotoxicity of different Nb<sub>2</sub>C formulations at various concentrations in vitro. Cell-counting kit-8 (CCK8) assay suggested that all Nb<sub>2</sub>C MXenes with different modifications did not cause a significant decrease in the RAW 264.7 macrophages viability even at a high concentration of 500  $\mu g \ mL^{-1}$  (Figure S2A, Supporting Information). We chose to apply US to RAW 264.7 macrophages with 200  $\mu g \ mL^{-1}$  of various Nb<sub>2</sub>C formulations 4 h post-incubation in the following in vitro experiments.

ROS generated by NOX of phagocytic leukocytes (e.g., monocytes and macrophages) is a fundamental biological process in regulating immune functions of innate cells under physiological conditions.<sup>[27]</sup> Yet, in the context of CVDs, NOX in the vascular endothelial cells is elevated by CVDs risk factors to produce excessive intracellular ROS, thereby increasing vascular oxidative stress.<sup>[27c]</sup> Consequently, overproduction of ROS by macrophages and endothelial cells contributes to atherogenesis. Considering the aforementioned CAT/SOD-mimicking properties of Nb<sub>2</sub>C-Pt nanozymes to clear diverse ROS under US treatment, we then studied whether Nb2C-Pt-PEG or Nb2C-Pt@HA-PEG nanozymes and their mediated SCT could attenuate the ROS production in RAW264.7 macrophages. Cells were pretreated with lipopolysaccharide (LPS) before incubation with a ROS probe 2',7'-dichlorodihydrofluorescein diacetate (DCFH-DA). DCFH-DA was loaded into macrophages and converted into non-fluorescent DCFH by deacetylation with intracellular esterase. Inflammatory RAW 264.7 macrophages were subjected to various treatments and the intracellular ROS oxidized DCFH to fluorescent 2',7'-dichlorofluorescein (DCF), serving as an indicator of ROS. Strong fluorescence was detected from LPS-treated RAW 264.7 macrophages by confocal laser scanning microscopy (CLSM) compared with naïve RAW 264.7 macrophages, suggesting an intracellular microenvironment with high levels of ROS (Figure S3, Supporting Information). Similarly strong green fluorescence was monitored in the US-treated macrophages while ≈60% and ≈80% of the fluorescent signals were quenched by Nb<sub>2</sub>C-Pt-PEG and Nb<sub>2</sub>C-Pt@HA-PEG nanozymes, respectively, suggesting both nanozymes exhibited distinguished antioxidative performance (Figure 3A,B). In particular, CLSM images from Nb<sub>2</sub>C-Pt@HA-PEG+US group showed the dimmest green fluorescence and the mean fluorescent intensity (MFI) from Nb<sub>2</sub>C-Pt@HA-PEG+US group was ≈50% less than that from Nb<sub>2</sub>C-Pt@HA-PEG group (Figure 3A,B). These results demonstrated that Nb<sub>2</sub>C-Pt@HA-PEG-mediated SCT owned outstanding antioxidative performance and US treatment boosted the catalytic properties of Nb<sub>2</sub>C-Pt@HA-PEG nanozymes in scavenging ROS. Furthermore, to quantitatively evaluate ROS-scavenging capacity of various treatments at cellular level, supplementary flow cytometric analysis of DCF-positive cells was conducted (Figure 3C; Figure S4, Supporting Information). In line with

previous CLSM observations, Nb<sub>2</sub>C-Pt@HA-PEG+US group showed the least DCF-positive macrophages, reinforcing the superior performance of Nb<sub>2</sub>C-Pt@HA-PEG-mediated SCT in eliminating ROS than all other treatments (Figure 3D).

Nanomedicines for scavenging endogenous ROS represent effective strategies to resolve macrophage inflammation in ROSassociated diseases by promoting the transition of classical inflammatory M1 phenotype into regenerative M2 phenotype.<sup>[28]</sup> Since we have demonstrated Nb<sub>2</sub>C-Pt@HA-PEG nanozyme as a desirable therapeutic agent against endogenous oxidative stress in macrophages under US irradiation, effects of scavenging ROS on regulating macrophage polarization would further provide comprehensive evidence for elucidating the regulatory effect of Nb<sub>2</sub>C-Pt@HA-PEG-mediated SCT during the development of atherosclerosis. To this end, the expression levels of M1 markers (TNF- $\alpha$ , IL-1 $\beta$  and IL-6) and M2 markers (Arg-1 and TGF- $\beta$ ) were quantified by quantitative real-time polymerase chain reaction (qRT-PCR) measurements.[29] To obtain M1 macrophages, RAW 264.7 macrophages were stimulated with LPS, resulting in substantial increase in the secretion of TNF- $\alpha$ , IL-1 $\beta$  and IL-6, which are pro-inflammatory effector molecules responsible for chronic inflammation related to atherosclerosis.[30] Arg-1, one of the most robust markers for M2 phenotype macrophages, is an anti-inflammatory enzyme for arginine metabolism in macrophage to manipulate immune responses in chronic atherosclerosis.[31] qRT-PCR results showed significant reduction in the expression of IL-1 $\beta$ and IL-6 from all treatment groups excluding pristine Nb2C group, possibly attributing to the inherent antioxidative effect of Nb<sub>2</sub>C-Pt-PEG and Nb<sub>2</sub>C-Pt@HA-PEG nanozymes. More importantly, Nb<sub>2</sub>C-Pt@PEG+US and Nb<sub>2</sub>C-Pt@HA-PEG+US groups revealed a notably superior efficacy in attenuating the expression of TNF- $\alpha$ , IL-1 $\beta$  and IL-6 than their counterparts without US irradiation while no significant difference was detected among all markers between Nb2C-PEG and Nb2C-PEG+US groups (Figure 3E-G). Collectively, these findings suggested that integration with PtNP conferred the antioxidative and anti-inflammatory properties to Nb2C MXenes under US treatment, rendering PtNP-deposited Nb<sub>2</sub>C MXenes a potential sonosensitizer for SCT. Of note, macrophages treated with Nb2C-Pt@HA-PEG+US not only showed the most pronounced inhibition in the expression of all three pro-inflammatory markers, but also showed the significantly higher expression of Arg-1 compared with all other groups (Figure 3E-H). No significant difference was detected in the expression of TGF- $\beta$  among all groups (Figure S5, Supporting Information). These data indicated that Nb2C-Pt@HA-PEGmediated SCT showed the most potent resolution of macrophage inflammation and regulated macrophage polarization to M2 antiinflammatory phenotype in vitro, potentiating this therapy for further attenuating the development of atherosclerosis in vivo. Since vascular endothelium system plays pivotal role during the development of atherosclerosis, we also evaluated biosafety profile and regulatory effects of Nb2C-Pt@HA-PEG-mediated SCT on vascular endothelial cells (ECs). Intracellular adhesion molecule 1 (ICAM-1) present on ECs contributes to recruiting circulating monocytes to leaky vascular endothelium, an early event in the atherogenesis. [32] As shown in Figure S2B (Supporting Information), all formulations of Nb<sub>2</sub>C MXenes did not exert cytotoxicity in human umbilical vein endothelial cell (HUVECs).

15214095, 0, Downloaded from https://advanced.onlinelibrary.wiley.com/doi/10.1002/adma.202420189 by HONG KONG POLYTECHNIC UNIVERSITY HU NG HOM, Wiley Online Library on [26.09/2025]. See the Terms

conditions) on Wiley Online Library for rules of use; OA articles are governed by the applicable Creative Commons License

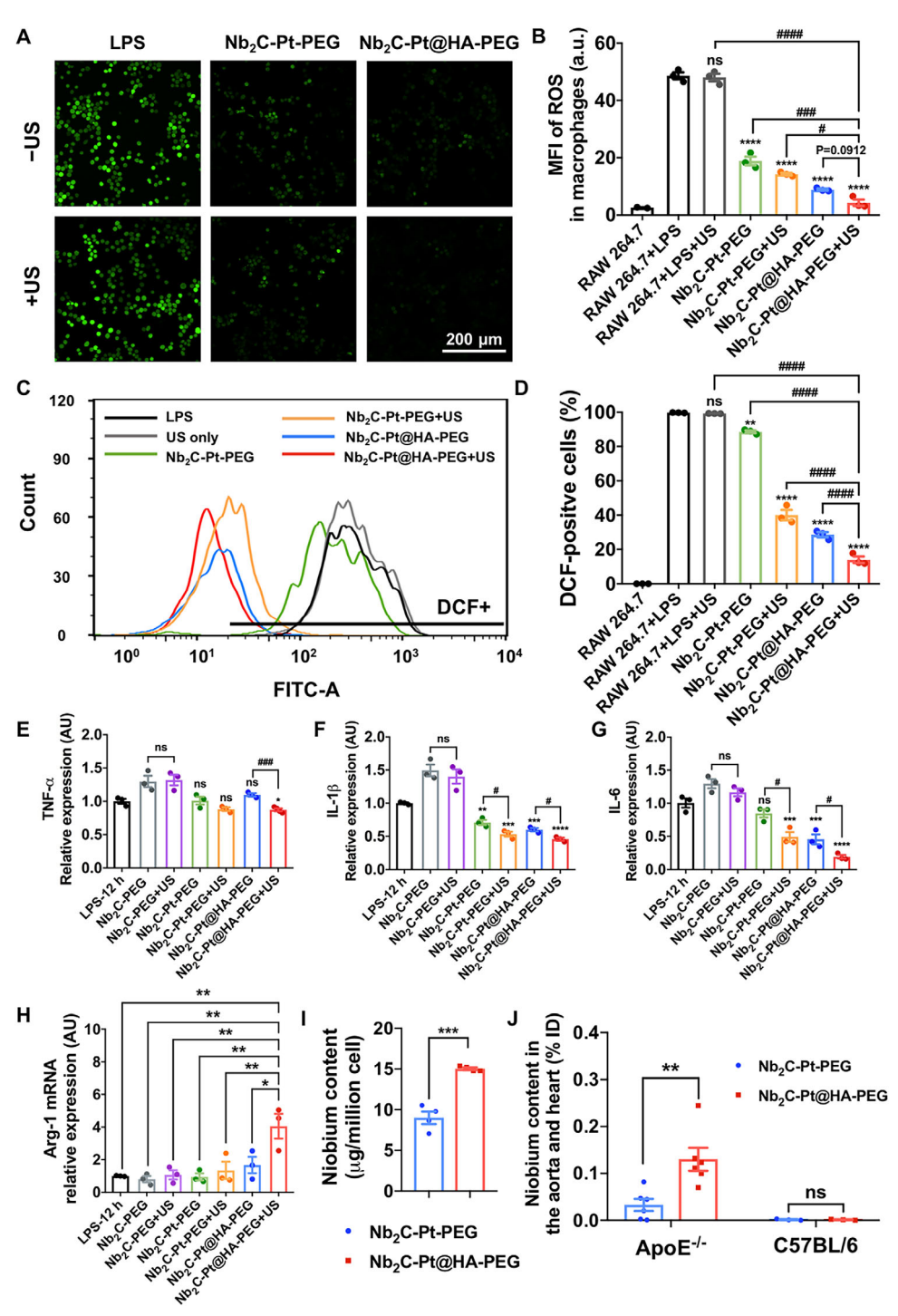


**Figure 3.** In vitro anti-atherosclerosis and in vivo plaque-targeting performance of Nb<sub>2</sub>C-Pt@HA-PEG nanosheets. A) Representative confocal fluorescence images of intracellular ROS detected by DCFH-DA assay and B) corresponding MFI in LPS-induced RAW 264.7 macrophages after various treatments (n = 3). C) Representative flow cytometry histograms of intracellular ROS stained by DCFH-DA and D) corresponding quantitative analysis. Data are presented as means  $\pm$  SEM. Statistical significance was calculated by one-way ANOVA with Tukey's test for post hoc analysis. ns: not significant (P > 0.05), \*\*P<0.01, \*\*\*\*P<0.001. #P<0.05, \*#P<0.001, ###P<0.0001. RT-qPCR analysis of M1 markers E) TNF-α, F) IL-1β, and G) IL-6 and M2 marker H) Arg-1 expression as an evaluation of the effect of scavenging ROS on the macrophage phenotypic transition after varied treatments in LPS-induced RAW 264.7 macrophages (n = 3). Data are presented as means  $\pm$  SEM. Statistical significance was calculated by one-way ANOVA with Tukey's test for post hoc analysis. ns: not significant (P > 0.05), \*P<0.05, \*\*P<0.01, \*\*\*P<0.001, \*\*\*\*P<0.0001. #P<0.05, ##P<0.001. I) In vitro uptake of Nb<sub>2</sub>C-Pt@HA-PEG by RAW 264.7 macrophages by ICP-MS measurements (n = 4). J) ICP-MS measurements of the Nb content in the aorta and heart harvested from plaque-bearing ApoE<sup>-/-</sup> mice and healthy C57BL/6 mice 4 h post-injection of Nb<sub>2</sub>C-Pt-PEG or Nb<sub>2</sub>C-Pt@HA-PEG (n = 3-6). Statistical significance was calculated by Student's t test. All the data are presented as mean  $\pm$  SEM. ns: not significant (P > 0.05). \*\*P<0.01, \*\*\*P<0.001.





www.advmat.de

Benefiting from the US-responsiveness of Nb<sub>2</sub>C-Pt@HA-PEG nanozymes, ECs treated with Nb<sub>2</sub>C-Pt@HA-PEG-mediated SCT showed a 28% lower expression of ICAM-1 than Nb<sub>2</sub>C-Pt@HA-PEG-treated cells. Additionally, we observed  $\approx\!30\%$  inhibition of pro-inflammatory ICAM-1 in Nb<sub>2</sub>C-Pt@HA-PEG+US-treated cells compared with Nb<sub>2</sub>C-Pt-PEG+US-treated cells, suggesting that the effective delivery of Nb<sub>2</sub>C-Pt@HA-PEG enhanced the suppression of marker gene related to vascular inflammation in the context of atherosclerosis (Figure S6A, Supporting Information).

Given that HA serves as targeting ligand for CD44 receptors on activated macrophages or ECs, the outstanding antiinflammatory effect of Nb<sub>2</sub>C-Pt@HA-PEG-mediated SCT likely stems from higher cellular uptake of Nb<sub>2</sub>C-Pt@HA nanozymes by inflammatory macrophages.<sup>[33]</sup> To verify the targeted delivery of HA-modified Nb2C MXenes to activated macrophages or ECs, we compared cellular niobium (Nb) contents in the cells after incubation with the same concentration of Nb<sub>2</sub>C-Pt-PEG or Nb<sub>2</sub>C-Pt@HA-PEG. Inductively coupled plasma mass spectrometry (ICP-MS) measurements showed that the amount of Nb in Nb<sub>2</sub>C-Pt@HA-PEG group was ≈1.5-fold of that in Nb<sub>2</sub>C-Pt-PEG group (Figure 3I). Although there was no significant difference in the cellular uptake between two nanostructures by HUVECs, the mean Nb contents in the cells in Nb<sub>2</sub>C-Pt@HA-PEG group showed a ≈25% increase than that in Nb<sub>2</sub>C-Pt-PEG group (Figure S6B, Supporting Information). These data not only demonstrated that modification of nanosheets with HA promoted delivery to inflammatory macrophages and ECs in vitro, but also encouraged us to further examine the ability of Nb2C-Pt@HA-PEG as a plaque-targeting nanozyme for alleviating atherosclerotic plaque in vivo.

# 2.4. In Vivo Plaque-Targeting and Anti-Atherosclerosis Efficacy of Nb<sub>2</sub>C-Pt@HA-PEG-Mediated SCT

For in vivo studies, we first examined the blood pharmacokinetics of Nb<sub>2</sub>C-Pt and Nb<sub>2</sub>C-Pt@HA-PEG following an i.v. injection into the plaque-bearing ApoE $^{-/-}$  mice, keeping the concentration of Nb injected at 10 mg Nb kg $^{-1}$  per mouse. ICP-MS measurements of Nb contents were performed in the blood samples extracted from different time points. The results showed that Nb<sub>2</sub>C-Pt@HA-PEG displayed biexponential decay kinetics with blood half-life (t<sub>1/2</sub>) of  $\approx$ 1.52 h while Nb<sub>2</sub>C-Pt showed a shorter half-life of 1.21 h, demonstrating that PEGylation increased the circulating time of Nb<sub>2</sub>C-Pt@HA-PEG (Figure S7, Supporting Information).

To demonstrate the preferential delivery of Nb<sub>2</sub>C-Pt@HA-PEG nanozymes to atherosclerotic plaques, we compared the organlevel distribution between Nb<sub>2</sub>C-Pt@PEG and Nb<sub>2</sub>C-Pt@HA-PEG. 4 h post-injection of both Nb<sub>2</sub>C MXenes into plaquebearing ApoE<sup>-/-</sup> mice, ICP-MS analysis of Nb contents in the aorta and heart showed evidently  $\approx$ threefold higher accumulation of Nb<sub>2</sub>C-Pt@HA-PEG (0.13% ID, percentage of injected dose) compared to their counterpart Nb<sub>2</sub>C-Pt@PEG (0.03% ID) (Figure 3J). Meanwhile, we did not observe a similar pattern of differential distribution in other major organs; both types of Nb<sub>2</sub>C MXenes accumulated abundantly in the liver and spleen, with limited accumulation in the kidneys (Figure S8, Support-

ing Information). Moreover, we probed the distribution of both Nb $_2$ C MXenes upon injection into non-atherosclerotic C57BL/6 mice and found similarly low Nb contents in the aorta and heart for both Nb $_2$ C-Pt@PEG and Nb $_2$ C-Pt@HA-PEG groups, which were much less than those in plaque-bearing mice (Figure 3J). Taken together, these results indicated that HA modification selectively promoted delivery of Nb $_2$ C MXenes to atherosclerotic plaques, endowing Nb $_2$ C-Pt@HA-PEG nanozymes with improved plaque-targeting capability in vivo. The accumulation of both nanosheets in the aorta and heart was progressively higher from 4 h post-injection to 24 h post-injection (Figure S9, Supporting Information). Thus, atherosclerotic mice were exposed to US at 24 h post-injection of Nb $_2$ C MXenes in the following efficacy studies.

Given that we have demonstrated the plaque-targeted delivery of Nb<sub>2</sub>C-Pt@HA-PEG nanozymes, we next investigated whether Nb<sub>2</sub>C-Pt@HA-PEG-mediated SCT exerted anti-atherosclerosis effect. Upon i.v. administration of Nb<sub>2</sub>C MXenes into plaquebearing ApoE<sup>-/-</sup> mice fed with high cholesterol diet (HCD) for 20 weeks, our treatment regimen took place every 3 days for total three times from week 21-22, keeping the amount of Nb injected constant across all groups (Figure 4A). Especially, for Nb<sub>2</sub>C-Pt-PEG+US and Nb<sub>2</sub>C-Pt@HA-PEG+US groups, we applied US irradiation 24 h post-injection of MXenes for 10 min. All mice were sacrificed 48 h after the final US treatment. First, we examined the efficacy of Nb<sub>2</sub>C-Pt@HA-PEG-mediated SCT on plaque size by staining whole aortas and aortic root sections with Oil Red O (ORO) (Figure 4B,C; Figure \$10, Supporting Information). The lesion areas in the whole aortas of mice from Nb<sub>2</sub>C-Pt@HA-PEG group (24.5%) were considerably smaller than those from untreated mice (32.4%) and US-treated mice (29.2%), indicating the inherent antioxidative properties of Nb2C-Pt@HA-PEG nanozymes (Figure 4H). Besides, the lesion areas in the whole aortas from Nb2C-Pt-PEG+US group (26.1%) and Nb<sub>2</sub>C-Pt@HA-PEG+US group (19.1%) were also significantly smaller than those from control groups, suggesting that the introduction of PtNP conferred US-responsiveness to both nanozymes (Figure 4H). These findings aligned with previous in vitro studies. Particularly, Nb<sub>2</sub>C-Pt@HA-PEG+US group showed significantly smaller plaque size than Nb2C-Pt@HA-PEG group in the whole aorta, reinforcing the merit of USenhanced SCT. Next, we found that the aortic root plaque areas of mice from Nb2C-Pt-PEG+US, Nb2C-Pt@HA-PEG, and Nb<sub>2</sub>C-Pt@HA-PEG+US groups were notably smaller than those from untreated mice and US-treated mice, with  $\approx$ 20%,  $\approx$ 15% and  $\approx$ 30% reduction, respectively (Figure 4I). Similarly, the aortic root area of Nb<sub>2</sub>C-Pt@HA-PEG+US group showed a ≈20% reduction compared with that of Nb<sub>2</sub>C-Pt@HA-PEG group. Overall, mice receiving Nb2C-Pt@HA-PEG-mediated SCT showed the smallest lesion area in both the entire aorta and the aortic root area among all treatment groups, which derives from promoted accumulation of Nb<sub>2</sub>C-Pt@HA-PEG nanozymes in the plaque and US-augmented sonocatalytic effects.

Next, we evaluated the effect of Nb<sub>2</sub>C-Pt@HA-PEG-mediated SCT on plaque stabilization since plaques at advanced stage with low collagen contents are prone to rupture, inducing subsequent thrombus formation and severe cardiovascular events.<sup>[34]</sup> Sirius Red staining of the aortic root showed thicker fibrous collagen cap around the plaques from Nb<sub>2</sub>C-Pt@HA-PEG+US group

www.advmat.de

15214095, 0, Downloaded from https://advanced.onlinelibrary.wiley.com/doi/10.1002/adma.202420189 by HONG KONG POLYTECHNIC UNIVERSITY HUNG HOM, Wiley Online Library on [2609/2025]. See the Terms and Conditions (https://onlinelibrary.wiley.

convierms-and-conditions) on Wiley Online Library for rules of use; OA articles are governed by the applicable Creative Commons License

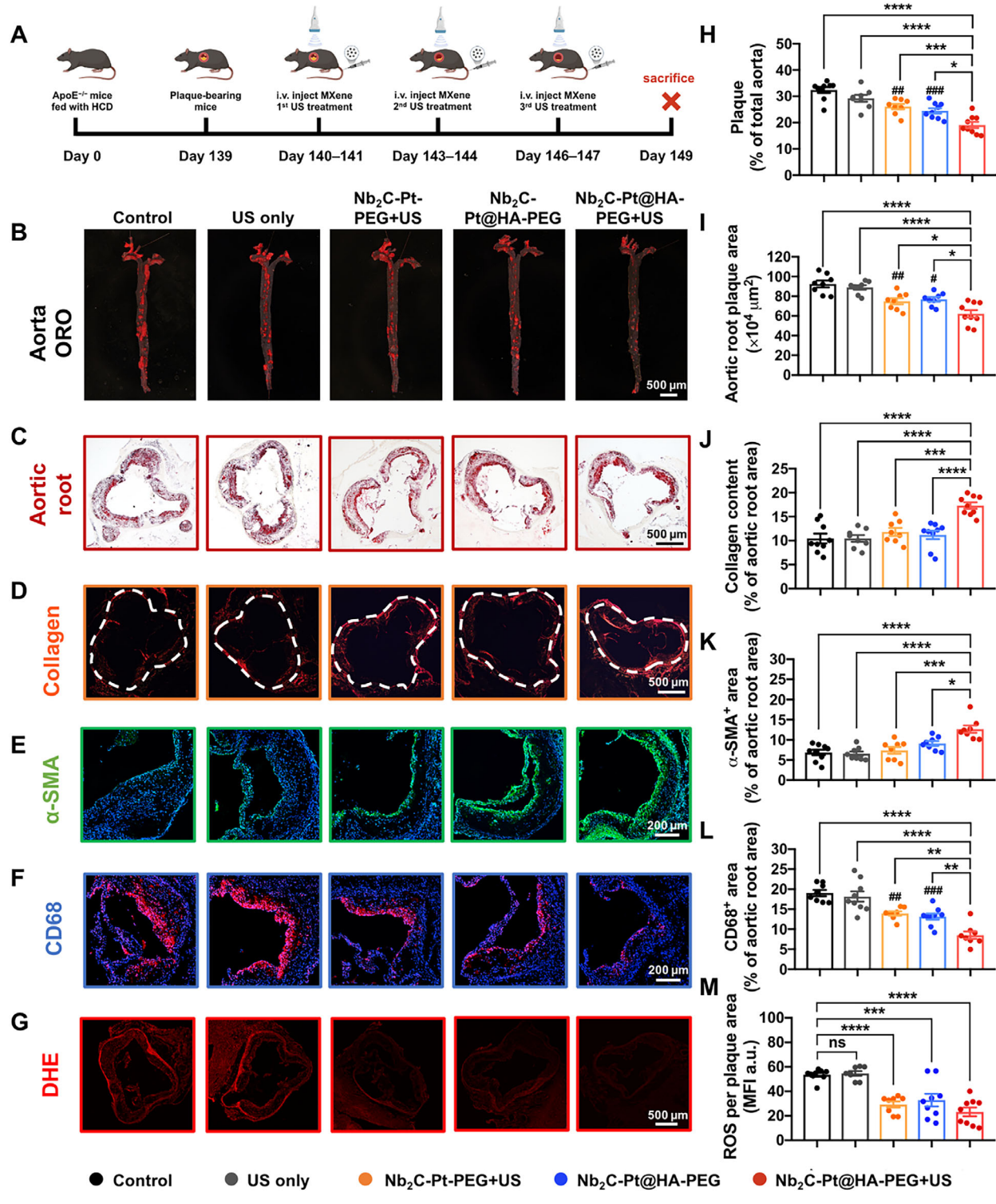


**Figure 4.** In vivo anti-atherosclerotic efficacy of Nb<sub>2</sub>C-Pt@HA-PEG-mediated SCT. A) Schematic illustration of in vivo Nb<sub>2</sub>C-Pt@HA-PEG-mediated SCT regimen. Representative images of B) Oil Red O (ORO)-stained intact aortas; C) ORO-stained aortic roots; D) Sirius Red-stained aortic roots (under polarized mode); immunofluorescent staining of E) α-SMA (Green: α-SMA, highly expressed by VSMCs; Blue: DAPI) and F) CD68 (Red: CD68, marker of monocytes and macrophages; Blue: DAPI); G) fluorescent staining of dihydroethidium (DHE) on aortic roots from various treatments (n = 8–9). Corresponding quantitative analysis of H) fractional plaque area in total aorta; I) plaque area, J) collagen content, contents of K) smooth muscle cells and L) monocytes and macrophages and M) mean fluorescence intensity (MFI) of intraplaque ROS in the aortic root. Data are presented as means  $\pm$  SEM. Statistical significance was calculated by one-way ANOVA with Tukey's test for post hoc analysis. ns: not significant (P > 0.05). \*P<0.05, \*\*P<0.01, \*\*\*\*P<0.001. \*P<0.05, \*\*P<0.001. \*\*\*\*P<0.001. \*\*\*\*P<0.001. \*\*\*\*P<0.001. \*\*\*\*P<0.001.



ADVANCED MATERIALS

www.advmat.de

(Figure 4D). Corresponding quantitative analysis revealed that the collagen content in Nb<sub>2</sub>C-Pt@HA-PEG+US group (17.3%) is notably higher than all other groups ( $\approx 10\%$ ) (Figure 41). Moreover, vascular smooth muscle cells (VSMCs), highly expressing  $\alpha$  smooth muscle actin ( $\alpha$ -SMA), are generators of extracellular matrix (such as collagen, elastin and proteoglycan) to stabilize the atherosclerosis by contributing to fibrous cap formation.[35] Immunofluorescent (IF) staining revealed obviously higher expression of α-SMA in the Nb<sub>2</sub>C-Pt@HA-PEGmediated SCT group than that in all other groups (Figure 4E; Figure S11, Supporting Information). The aortic  $\alpha$ -SMA-positive area for the Nb<sub>2</sub>C-Pt@HA-PEG+US group is ≈1.5-fold of that in other groups (Figure 4K), suggesting a more stabilized plaque phenotype and matching the observed elevation in collagen deposition in the previous Sirius Red staining (Figure 4D). In addition, sections of aortic root from mice receiving Nb<sub>2</sub>C-Pt@HA-PEG-mediated SCT showed the smallest size of the necrotic core, a key contributor to atherosclerotic plaque vulnerability and rupture, among various treatments (Figure \$12, Supporting Information).[36] Consequently, these data indicated that Nb<sub>2</sub>C-Pt@HA-PEG nanozymes effectively alleviated atherosclerosis by shrinking plaque areas in whole aorta and aortic root in vivo, echoing our previous in vitro qRT-PCR results. Furthermore, Nb<sub>2</sub>C-Pt@HA-PEG-mediated SCT not only reduced plaque area but also promoted a shift toward a more stable phenotype, characterized by a thicker and intact fibrous cap, elevated collagen deposition and smaller necrotic core areas, which helps to prevent secondary necrosis and reduces the risk of plaque rupture.

# 2.5. Mechanism of Anti-Atherosclerosis Effect of Nb<sub>2</sub>C-Pt@HA-PEG-Mediated SCT

During the initiation stage of atherosclerosis, leukocytes are recruited to the subendothelium due to the elevated expression of chemokines and adhesion molecules, and facilitated by increased permeability of a dysfunctional endothelium.[37] This infiltration of circulating leukocytes into the lesion area significantly contributes to atherosclerosis progression. Therefore, to further explore the mechanisms responsible for the anti-atherosclerosis effect of Nb<sub>2</sub>C-Pt@HA-PEG-mediated SCT, we first examined the inflammatory cell contents in the aortic root. Immunostaining of CD68 (an indicator of monocytes and macrophages) showed smaller CD68-positive regions in the aortic root sections from Nb<sub>2</sub>C-Pt-PEG+US, Nb<sub>2</sub>C-Pt@HA-PEG, and Nb<sub>2</sub>C-Pt@HA-PEG+US groups than control group and US-treated group (Figure 4F; Figure S13, Supporting Information). Corresponding semi-quantitative analysis of the fluorescence signals from the aortic CD68-positive areas in proportion to the entire aortic root area further demonstrated that Nb<sub>2</sub>C-Pt-PEG+US (13.9%), Nb<sub>2</sub>C-Pt@HA-PEG (13.2%), and Nb<sub>2</sub>C-Pt@HA-PEG+US group (8.5%) showed significantly lower macrophage content than control group (19.0%) and US-treated group (18.2%) (Figure 4L), suggesting that both nanozymes inhibited macrophage infiltration under US irradiation. The strongest anti-atherosclerosis effect of Nb<sub>2</sub>C-Pt@HA-PEG-mediated SCT was derived from plaque-targeted delivery and US-enhanced sonocatalytic effect.

To further examine whether the potent anti-atherosclerotic effect of Nb<sub>2</sub>C-Pt@HA-PEG+US is due to its ROS-scavenging effect, we measured the intra-plaque ROS level by live staining of dihydroethidium (DHE) which mainly measures superoxide, in the aortic root sections from ApoE<sup>-/-</sup> mice subjected to different treatments. CLSM observations showed the lowest fluorescent intensity of DHE in the sections from Nb<sub>2</sub>C-Pt@HA-PEG+US group, suggesting the strongest effect to suppress intraplaque ROS level (Figure 4G; Figure S14, Supporting Information). Quantitative analysis further confirmed that Nb2C-Pt@HA-PEGmediated SCT remarkably attenuated oxidative stress with aortic plaque by diminishing ≈60% ROS compared with untreated or US-treated groups (Figure 4M). Consistent with the potent ROS-scavenging capability of Nb<sub>2</sub>C-Pt@HA-PEG under US irradiation in our in vitro studies, these findings supported the notion that Nb<sub>2</sub>C-Pt@HA-PEG-mediated SCT performed anti-atherosclerosis effect via regulating intraplaque redox homeostasis.

Nevertheless, to gain deeper mechanistic insights into the antiatherosclerosis molecular mechanism of Nb2C-Pt@HA-PEGmediated SCT, we performed bulk RNA sequencing on the total RNA from LPS-induced inflammatory RAW 264.7 macrophages that received treatments of "Nb2C MXenes", "Nb2C-Pt@HA-PEG", or "Nb<sub>2</sub>C-Pt@HA-PEG+US" (n = 3) for further RNAseq analysis. For pairwise comparisons, we identified differentially expressed genes (DEGs) with statistical significance of Padjust < 0.05. First, we used the Upset diagram and bar chart to show the overview of DEGs in each pairwise comparison (Figure S15, Supporting Information). Representative DEGs related to pathogenesis of atherosclerosis (e.g., Il6,[38] Ccl5,[39] Cd36,[40] Abca1,<sup>[41]</sup> and Cxcl2<sup>[42]</sup>) were illustrated by heatmap diagram (Figure 5A). There was a total of 145 DEGs detected in Pair 6 ("Nb<sub>2</sub>C-Pt@HA-PEG+US" vs "Model"), including 127 downregulated genes and 18 upregulated genes distributed in volcano plot (Figure 5B). Significantly more DEGs from this comparison than all other 5 pairwise comparisons suggested that the effect of Nb<sub>2</sub>C-Pt@HA-PEG-mediated SCT was the strongest against atherosclerosis, supporting the additive efficacy of antioxidative Nb2C-Pt@HA-PEG nanozymes and US-amplified sonocatalytic effect. In the following analyses, we mainly focused on the pairwise comparison between the "Nb<sub>2</sub>C-Pt@HA-PEG+US" and "Model" groups to investigate the athero-protective effect and mechanism of Nb<sub>2</sub>C-Pt@HA-PEG-mediated SCT. Gene ontology (GO) terms were applied to identify the biological processes related to atherosclerosis, which showed significant change in processes including "reactive oxygen species metabolic process"; "lipid homeostasis"; "regulation of apoptotic process", "positive regulation of aortic smooth muscle cell differentiation", etc. (Figure 5C). In addition, Kyoto Encyclopedia of Genes and Genomes (KEGG) pathways most related to atherosclerosis are also identified including: "TNF signaling pathway"; "NF-κappa B signaling pathway"; "IL-17 signaling pathway"; "Lipid and atherosclerosis"; "Toll-like receptor signaling pathway"; "FoxO signaling pathway"[43]; "Apoptosis" and "PPAR signaling pathway" (Figure 5D). These results aligned with the downregulation of TNF-α, IL-1β, and IL-6 by qRT-PCR by Nb<sub>2</sub>C-Pt@HA-PEGmediated SCT (Figure 3E-G). All three cytokines are critical players in the "TNF signaling pathway" and "NF-kappa B signaling pathway" showed in Figure 5D. In addition, some top signals on

wiley.com/doi/10.1002/adma.202420189 by HONG KONG POLYTECHNIC UNIVERSITY HU NG HOM, Wiley Online Library on [26/09/2025]. See the Terms

on Wiley Online Library for rules of use; OA articles are governed by the applicable Creative Commons

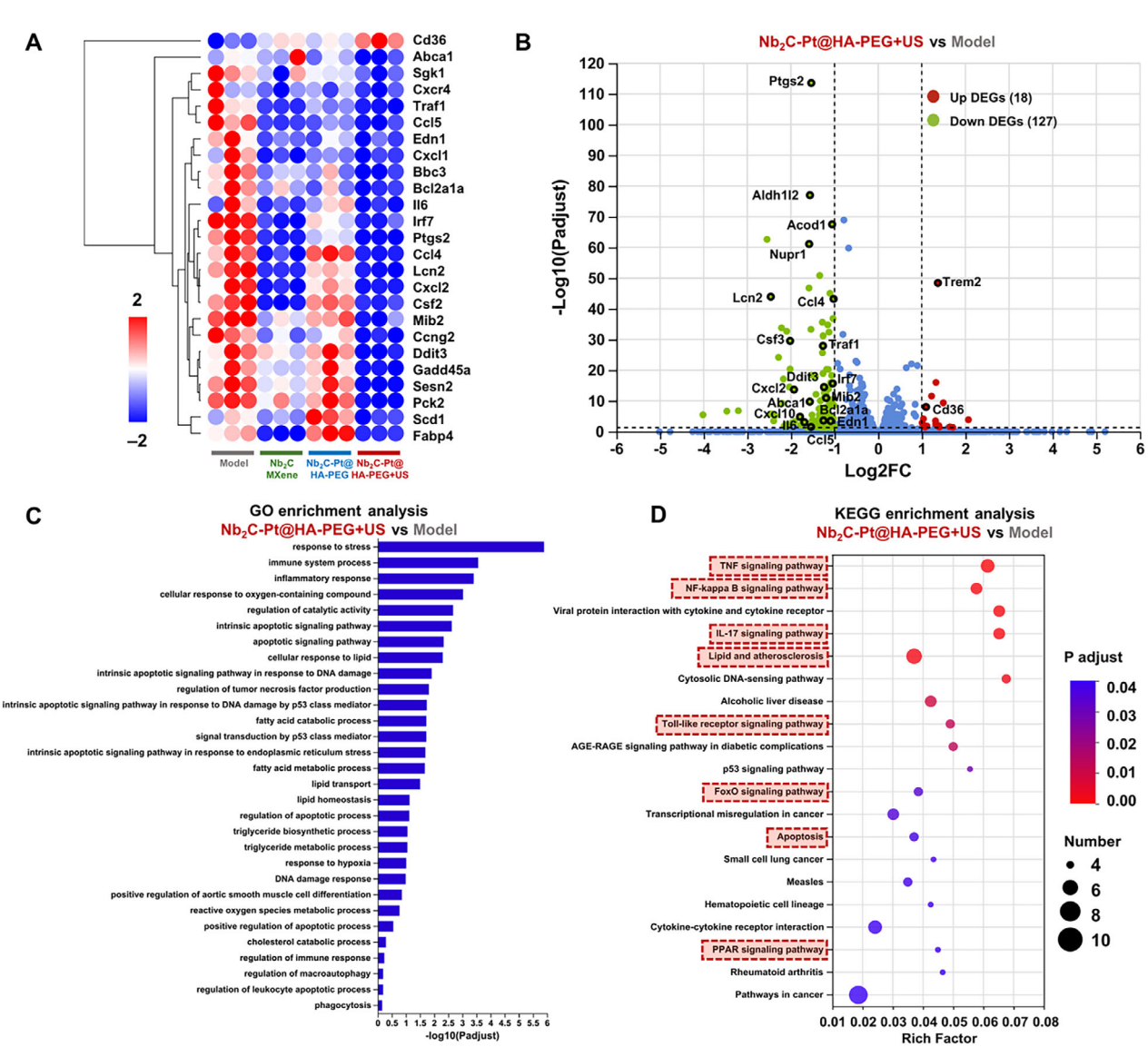


Figure 5. Mechanism study of Nb<sub>2</sub>C-Pt@HA-PEG nanozymes for alleviating atherosclerosis by transcriptome high throughput sequencing. A) Heatmap diagram of representative DEGs after various treatments compared to the "model group" (LPS induced inflammatory RAW 264.7 macrophages). B) Volcano plot showing the distribution of upregulated DEGs (red) and downregulated DEGs (green) with absolute fold change > 2 and Padjust value < 0.05 by comparing "Nb2C-Pt@HA-PEG+US" group with "model group". C) Key statistically enriched GO terms found by comparing "Nb2C-Pt@HA-PEG+US" group to the "model group" in biological processes related to atherosclerosis. D) KEGG pathway enrichment analysis from DEGs in "Nb2C-Pt@HA-PEG+US" group compared to the "model group". n = 3 per group.

the volcano plot in Figure 5B, such as Ptgs2 encoding COX-2, a major vascular oxidative enzyme, is associated with "reactive oxygen species metabolic process" and "IL-17 signaling pathway", which was previously identified to be clinically positively correlated with the severity of atherosclerosis. [44] In addition, Ptgs2 is related to ferroptosis and abundantly expressed in the inflammatory sites. [44a,45] Cd36, which is another top signal, associated with "PPAR signaling pathway", was upregulated in Nb2C-Pt@HA-PEG+US group. CD36 is a lipid transporter, whose upregulation dampens atherogenic inflammatory responses by removing denatured lipoproteins or chylomicron in the blood to prevent hyperlipidemia. [46] Nb<sub>2</sub>C-Pt@HA-PEG-mediated SCT also substantially downregulated the expression of Irf7 from "Lipid and atherosclerosis", which is a main mediator of autoinflammatory responses.<sup>[47]</sup> Overall, RNA-seq analysis suggested that the athero-protective effect of Nb<sub>2</sub>C-Pt@HA-PEG-mediated SCT is associated with dampening inflammatory responses, promoting efferocytosis, suppressing lipid uptake, and restoring redox homeostasis within the vascular microenvironment.

#### 2.6. In Vivo Biosafety Evaluation of Nb<sub>2</sub>C-Pt@HA-PEG-Mediated SCT

To investigate the biocompatibility and translational potential of Nb<sub>2</sub>C-Pt@HA-PEG-mediated SCT, we initially monitored body





vww advmat de

weights of mice from various treatment groups during the full treatment period and observed no significant differences among all treatment groups (Figure 6A). There were no significant differences in a series of hematological parameters, including white blood cells (WBC), neutrophils, lymphocytes and monocytes among various treatment groups (Figure 6B). Although the red blood cells (RBC) in US-treated mice were significantly more than those in the mice from Nb<sub>2</sub>C-Pt-PEG+US treatment group, the RBC count was still within the normal range (6.5-11.5 × 10<sup>6</sup>/μL). Additionally, no significant differences were detected in the levels of serum alanine transaminase (ALT), aspartate aminotransferase (AST), albumin, globulin and blood urea nitrogen (BUN) and creatinine (CRE), indicating that Nb<sub>2</sub>C-Pt@HA-PEG-mediated SCT did not affect hepatic and renal functions (Figure 6C). Finally, Nb2C-Pt@HA-PEG-mediated SCT also did not change the weights (Figure S16, Supporting Information) or morphological structure of major internal organs such as heart, liver, spleen and kidneys (Figure 6D). Furthermore, to examine the possible side effects of Nb<sub>2</sub>C-Pt@HA-PEG-mediated SCT on mice, long-term biosafety profile was evaluated 4 weeks after the last US treatment. There was ≈50% reduction in the Nb contents from liver harvested from mice 4 weeks after full treatment compared with that collected from mice 24 h after single injection, suggesting the pronounced clearance of Nb<sub>2</sub>C-Pt@HA-PEG nanosheets from body (Figure S17, Supporting Information). There were no significant differences in blood hematological parameters (Figure S18, Supporting Information), biochemical parameters (Figure \$19, Supporting Information) and histological structure (Figure \$20, Supporting Information). On the basis of the practices mentioned above, Nb<sub>2</sub>C-Pt@HA-PEGmediated SCT regressed and stabilized plaque without causing severe cytotoxicity, providing a novel but safe strategy for treating atherosclerosis.

#### 3. Conclusion

In summary, we have developed a Nb<sub>2</sub>C-Pt@HA-PEG nanozyme-mediated SCT for targeted delivery to the plaque and treatment of atherosclerotic CVDs. This nanozyme exhibited a dual enzyme-mimicking and US-responsive properties. In terms of enzyme-like activities, Nb2C-Pt@HA-PEG showed antioxidative properties comparable to CAT and SOD, which effectively diminished ROS production and dampened inflammatory responses during atherogenesis. In terms of its US-responsiveness, Nb2C-Pt@HA-PEG nanozymes exhibited boosted sonocatalytic performance upon US irradiation in scavenging ROS and suppressing oxidative stress-induced inflammation. In addition, we have demonstrated that Nb2C-Pt@HA-PEG nanozymes selectively targeted atherosclerotic plaques, achieving approximately fourfold accumulation compared to the Nb<sub>2</sub>C-Pt@PEG group. This significant targeted delivery underscored the advantage of utilizing HA as targeting ligands for lesional macrophages. Regarding the in vivo efficacy, Nb2C-Pt@HA-PEG nanozymes effectively reduced plaque area in both aorta and aortic root, while Nb2C-Pt@HA-PEGmediated-SCT outperformed Nb2C-Pt@HA-PEG by a further reduction in both whole agrta plague area and agrtic root plague area. Importantly, it also promotes plaque stability, characterized by a thicker fibrous cap and a smaller necrotic core. Besides,

Nb<sub>2</sub>C-Pt@HA-PEG-mediated SCT overcame the cytotoxicity typically associated with conventional preparation of MXene, which was achieved by hydrofluoric acid etching. RNA-seq further supported that therapeutic effect of Nb<sub>2</sub>C-Pt@HA-PEGmediated SCT for atherosclerosis are attributed to: eliminating intraplaque ROS production, inhibiting monocyte-macrophage infiltration, dampening inflammatory responses, regulating lipid metabolism and promoting efferocytosis. Some nanomaterials are known to exhibit multienzyme-like activities including SOD, CAT and peroxidase (POD). [48] We have followed previous methods and determined that our Nb<sub>2</sub>C-Pt@HA-PEG nanozyme exhibited a specific POD-like activity of ≈2 U mg<sup>-1</sup> under US irradiation. [49] Despite US treatment boosts the catalytic activities of Nb<sub>2</sub>C-Pt@HA-PEG nanozyme, it still underperforms its natural counterparts or single-atom nanozymes (SAzymes).<sup>[50]</sup> We are supposed to engineer the active metal center or alter the electronic coordination environment in the future work to further improve the catalytic efficiency of nanozymes. Nevertheless, our study provided valuable insights into the possible application of ROS-scavenging MXenes-mediated SCT for treating other oxidative stress-associated inflammatory diseases such as rheumatoid arthritis, acute organ injury, obesity and insulin resistance, and neurodegenerative diseases.<sup>[51]</sup> Considering that our approach only requires a portable commercial US device to achieve deep-seated sonocatalytic efficacy, our Nb2C-Pt@HA-PEG-mediated SCT also holds promising translational potential compared with other near-infrared light-triggered photothermal or photodynamic therapies.

## 4. Experimental Section

For detailed Experimental Section, please see SI Appendix.

Synthesis of  $Nb_2C$ -Pt: 5 mL single-layered  $Nb_2C$  MXene (1 mg mL<sup>-1</sup>) suspension reacted with 1 mL  $H_2$ PtCl $_6$  aqueous solution (8 mM) and 1.5 mL sodium citrate (40 mM) for 30 min at 100 °C. The product was collected by centrifugation at 12000 rpm for 10 min and resuspended in deionized (D.I.) water and this step was repeated for three times. To prepare the  $H_2$ PtCl $_6$  aqueous solution (8 mM), 1 mL PtCl $_4$  (40 mM) was added into 4 mL HCl (20 mM) at room temperature.

HA Modification: First, to modify amine groups to MXenes, 10 mg Nb<sub>2</sub>C-Pt and 10 μL of APTES were dispersed into 10 mL ethanol and stirred for 10 min. After refluxing for 24 h, Nb<sub>2</sub>C-Pt-NH<sub>2</sub> were obtained by centrifugation and washed with D.I. water for three times. Amine-modified Nb<sub>2</sub>C-Pt were covalently attached to carboxylate-terminated HA. Briefly, to activate carboxyl groups of HA, 40 μmol of EDC, 10 μmol of NHS and 10 μmol of HA (molecular weight: 70–120 KDa, H10018, SAITONG) were added into 10 mL of PBS and stirred for 30 min. Next, 10 mg of Nb<sub>2</sub>C-Pt-NH<sub>2</sub> were added to the reaction mixture and left stirring overnight. Nb<sub>2</sub>C-Pt@HA were obtained by centrifugation and washed with D.I. water for three times.

Synthesis of  $Nb_2C$ -Pt@HA-PEG: Typically, 10 mg  $Nb_2C$ -Pt@HA were dissolved in 30 mL of DSPE-PEG<sub>2000</sub> solution (1 mg mL<sup>-1</sup>, Macklin) and sonicated for 2 h.  $Nb_2C$ -Pt@HA-PEG were collected by centrifugation and washed with D.I. water for three times. PEG-coated  $Nb_2C$  ( $Nb_2C$ -PEG) and  $Nb_2C$ -Pt ( $Nb_2C$ -Pt-PEG) were processed under same procedure with  $Nb_2C$ -Pt@HA-PEG.

*Animal Model*: All animal procedures followed the existing guidelines stipulated by the Animal Subjects Ethics Sub-committee (ASESC) at The Hong Kong Polytechnic University (PolyU) (ASESC Case No. 23–24/632-AP-R-CRF). ApoE<sup>-/-</sup> mice were purchased from GemPharmatech and shipped to PolyU Shenzhen Institute. ApoE<sup>-/-</sup> male mice (8 weeks old) fed with a high cholesterol diet (HCD, 108c, Jiangsu Xietong

1521/0495, 0, Downloaded from https://advanced.onlinelibrary.wiely.com/doi/10.1002/adma.202420189 by HONG KONG POLYTECHNIC UNIVERSITY HU NG HOM, Wiley Online Library on [26/09/2025]. See the Terms

nditions) on Wiley Online Library for rules of use; OA articles are governed by the applicable Creative Commons L

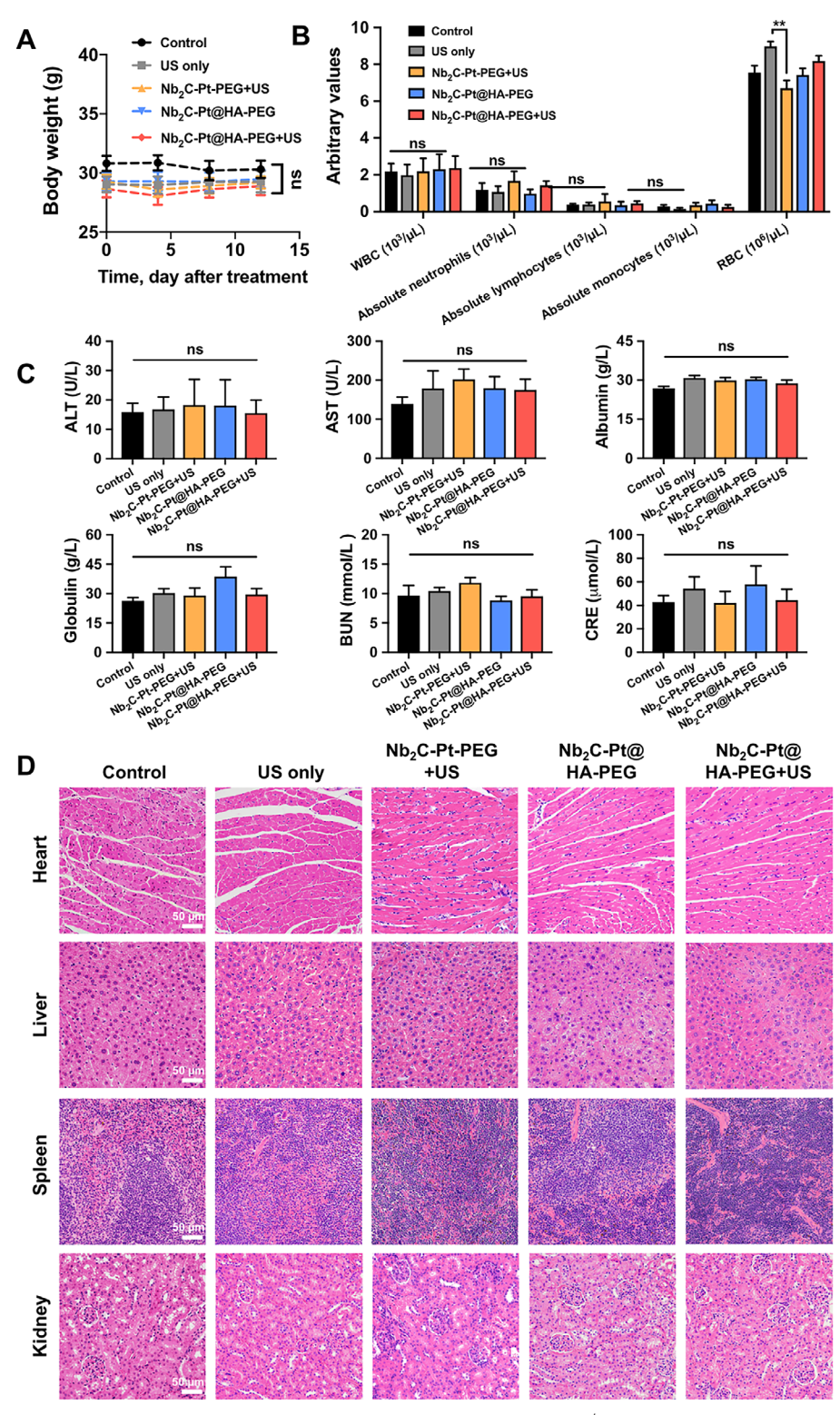


Figure 6. In vivo toxicity of various types of MXenes following a complete treatment in ApoE $^{-/-}$  mice. A) Body weight of mice from various groups throughout the treatment. B) Blood cell composition measured by complete blood count (CBC) test including white blood cell (WBC), absolute neutrophils, lymphocytes, monocytes and red blood cell (RBC). C) Levels of serum ALT, AST, albumin and globulin (markers for liver function) and BUN and CRE (markers for kidney function). Data are presented as means  $\pm$ SEM. Statistical significance was calculated by one-way ANOVA with Tukey's Test for post-hoc analysis. ns: not significant (P > 0.05), \*\*P < 0.01. n = 4–5 mice per group, across two experiments. D) Histological examination of the heart, liver, spleen, and kidneys harvested from ApoE $^{-/-}$  mice with advanced atherosclerotic plaques that were subject to different treatments. Representative images were chosen from n = 8–9 mice per group, across three experiments.



www.advmat.de

Pharmaceutical Bio-engineering Co., Ltd.) for 20 weeks to induce the formation of atherosclerotic plaques in the aorta and aortic root were randomly divided into various treatment groups of 8–9 animals each. The group size (N) was calculated based on Dunnett's formalism and power calculation ( $\alpha=0.05$ , power = 0.80). In brief,  $\mu=\sqrt{N}\times\delta/\sigma$ , where  $\mu$  is the correlation coefficient that depends on the size of each group. With four different treatment groups,  $\mu$  is 4.46. $^{[52]}$  If the superior treatment group gives an outcome ( $\delta$ ) of 1.5 SD ( $\sigma$ ) better than the control group, the required size of N is  $(4.46 \div 1.5)^2 = 8.84$ , or equivalently 8–9 mice per group.

Data Processing and Statistical Analysis: The Prism 8 (GraphPad Software) and Excel software were used for data analysis and graph construction. To determine the statistical significance in the comparison of two groups, an unpaired two-tail t test was performed. To determine the statistical significance in the comparison of multiple groups, an unpaired one-way analysis of variance (ANOVA) was performed with Tukey's Test for post hoc analysis. Normality of sampling distribution of means was validated by Shapiro-Wilk test. Homogeneity of variance was validated by Bartlett's test. Results are considered significant at P < 0.05.

## **Supporting Information**

Supporting Information is available from the Wiley Online Library or from the author.

## Acknowledgements

This work was supported by grants from the Research Grants Council of the Hong Kong Special Administrative Region, China (Project GRF No. 15303123, PolyU SRFS 2122–5S02, HKPDFS Ref. PDFS2324-5S09), and PolyU Grants (1-W30M, 1-CE0H, 1-CD7V, 1-YWC0, 1-CE0M). Q.B. thanks Zhang Lei for guidance in revising the manuscript and Hong Huiling for guidance in culturing HUVEC cells.

#### **Conflict of Interest**

The authors declare no conflict of interest.

### **Data Availability Statement**

The data that support the findings of this study are available from the corresponding author upon reasonable request.

#### **Keywords**

2D materials, cardiovascular diseases, fluoride-free MXene, nanomedicine, sonocatalytic therapy

Received: December 22, 2024 Revised: May 31, 2025 Published online:

- [1] A. Gisterå, G. K. Hansson, Nat. Rev. Nephrol. 2017, 13, 368.
- [2] a) H. Li, S. Horke, U. Förstermann, Atherosclerosis 2014, 237, 208;
  b) A. J. Kattoor, N. V. K. Pothineni, D. Palagiri, J. L. Mehta, Curr. Atheroscler. Rep. 2017, 19, 42.
- [3] D. Harrison, K. K. Griendling, U. Landmesser, B. Hornig, H. Drexler, Am. J. Cardiol. 2003, 91, 7.

- [4] a) W. N. Nowak, J. Deng, X. Z. Ruan, Q. Xu, Arterioscler. Thromb. Vasc. Biol. 2017, 37, 41; b) A. Pirillo, G. D. Norata, A. L. Catapano, Mediators Inflamm 2013, 2013, 152786; c) P. Marchio, S. Guerra-Ojeda, J. M. Vila, M. Aldasoro, V. M. Victor, M. D. Mauricio, Oxid. Med. Cell. Longev. 2019, 2019, 8563845.
- [5] Y. Wang, G. Z. Wang, P. S. Rabinovitch, I. Tabas, Circ. Res. 2014, 114, 421.
- [6] K. M. Channon, Arterioscler. Thromb. Vasc. Biol. 2002, 22, 1751.
- [7] M. Zandieh, J. Liu, Adv. Mater. 2024, 36, 2211041.
- [8] a) Z. He, W. Chen, K. Hu, Y. Luo, W. Zeng, X. He, T. Li, J. Ouyang, Y. Li, L. Xie, Y. Zhang, Q. Xu, S. Yang, M. Guo, W. Zou, Y. Li, L. Huang, L. Chen, X. Zhang, Q. Saiding, R. Wang, M. R. Zhang, N. Kong, T. Xie, X. Song, W. Tao, Nat. Nanotechnol. 2024, 19, 1386; b) R. Hu, C. Dai, C. Dong, L. Ding, H. Huang, Y. Chen, B. Zhang, ACS Nano 2022, 16, 15959; c) H. He, Q. Han, S. Wang, M. Long, M. Zhang, Y. Li, Y. Zhang, N. Gu, ACS Nano 2023, 17, 14555; d) X. Fu, X. Yu, J. Jiang, J. Yang, L. Chen, Z. Yang, C. Yu, Nat. Commun. 2022, 13, 6528.
- [9] J. Shan, L. Du, X. Wang, S. Zhang, Y. Li, S. Xue, Q. Tang, P. Liu, Adv. Sci. 2024, 11, 2304441.
- [10] a) K. Li, S. Wang, C. Chen, Y. Xie, X. Dai, Y. Chen, S. biomaterials, Co-ordin. Chem. Rev. 2025, 522, 216242; b) X. Qian, Y. Zheng, Y. Chen, Adv. Mater. 2016, 28, 8097; c) J. Guo, X. Pan, C. Wang, H. Liu, Bioconjug. Chem. 2021, 33, 993.
- [11] a) B. Lu, Z. Zhu, B. Ma, W. Wang, R. Zhu, J. Zhang, Small 2021, 17, 2100946; b) H. Lin, Y. Chen, J. Shi, Adv. Sci. 2018, 5, 1800518; c)
   M. Song, S. Y. Pang, F. Guo, M. C. Wong, J. Hao, Adv. Sci. 2020, 7, 2001546.
- [12] a) C. E. Shuck, K. Ventura-Martinez, A. Goad, S. Uzun, M. Shekhirev, Y. Gogotsi, ACS Chem. Health Safe. 2021, 28, 326; b) M. Dalamaga, K. Karmaniolas, A. Nikolaidou, E. Papadavid, J. Burn Care Res. 2008, 29, 541.
- [13] a) S. Y. Pang, Y. T. Wong, S. Yuan, Y. Liu, M. K. Tsang, Z. Yang, H. Huang, W. T. Wong, J. Hao, J. Am. Chem. Soc. 2019, 141, 9610; b) S. Y. Pang, W. F. Io, J. Hao, Adv. Sci. 2021, 8, 2102207.
- [14] a) Y. Zhu, Z. Wang, R. Zhao, Y. Zhou, L. Feng, S. Gai, P. Yang, ACS Nano 2022, 16, 3105; b) Y. Liang, C. Liao, X. Guo, G. Li, X. Yang, J. Yu, J. Zhong, Y. Xie, L. Zheng, J. Zhao, Small 2023, 19, 2205511; c) Y. Chen, C. Rong, W. Gao, S. Luo, Y. Guo, Y. Gu, G. Yang, W. Xu, C. Zhu, L. L. Qu, J. Colloid Interface Sci. 2024, 653, 540.
- [15] a) R. Zhou, M. Chang, M. Shen, Y. Cong, Y. Chen, Y. Wang, Adv. Sci. 2023, 10, 2301764; b) V. Deepagan, D. G. You, W. Um, H. Ko, S. Kwon, K. Y. Choi, G. R. Yi, J. Y. Lee, D. S. Lee, K. Kim, I. C. Kwon, J. H. Park, Nano Lett. 2016, 16, 6257.
- [16] H. Tong, H. L. Li, X. G. Zhang, Carbon 2007, 45, 2424.
- [17] A. Talo, J. Lahtinen, P. Hautojärvi, Appl. Catal. B: Environ. 1995, 5, 221.
- [18] a) Q. Bai, Y. Xiao, H. Hong, X. Cao, L. Zhang, R. Han, L. K. C. Lee, E. Y. Xue, X. Y. Tian, C. H. J. Choi, *Proc. Natl. Acad. Sci. USA* 2022, 119, 2201443119; b) L. Zhang, X. Y. Tian, C. K. W. Chan, Q. Bai, C. K. Cheng, F. M. Chen, M. S. H. Cheung, B. Yin, H. Yang, W. Y. Yung, Z. Chen, F. Ding, K. C. F. Leung, C. Zhang, Y. Huang, J. Y. W. Lau, C. H. J. Choi, *ACS Appl. Mater. Interfaces* 2018, 11, 13888.
- [19] E. Niki, Biol. Med. 2014, 66, 3.
- [20] D. A. MacInnes, J. Am. Chem. Soc. 1914, 36, 878.
- [21] a) M. Mittal, M. R. Siddiqui, K. Tran, S. P. Reddy, A. B. Malik, *Antioxid. Redox Signal.* **2014**, *20*, 1126; b) E. Graf, J. R. Mahoney, R. G. Bryant, J. W. Eaton, *J. Biol. Chem.* **1984**, *259*, 3620.
- [22] K. E. El-Kelany, S. Abdel-Azeim, O. Kühn, A. Elzatahry, M. F. Shibl, ACS Appl. Nano Mater. 2023, 6, 14040.
- [23] a) J. Mao, J. He, W. F. Io, F. Guo, Z. Wu, M. Yang, J. Hao, ACS Nano 2024, 18, 30360; b) V. A. Cao, M. Kim, S. Lee, C. G. Kim, P. Cao Van, T. N. Thi, J. R. Jeong, J. Nah, ACS Appl. Mater. Interfaces 2022, 14, 26824; c) D. Tan, C. Jiang, N. Sun, J. Huang, Z. Zhang, Q. Zhang, J. Bu, S. Bi, Q. Guo, J. Song, Nano Energy 2021, 90, 106528; d) C. Jiang, L. Zeng, D. Tan, P. Yan, N. Sun, Q. Guo, Z. Zhang, Z. Tao, C. Fang, R. Ji, H. Sun, R. Xu, Nano Energy 2023, 114, 108670.



ADVANCED MATERIALS

www.advmat.de

- [24] W. Baur, Acta Crystallogr. B. 1974, 30, 1195.
- [25] J. Zhang, Y. Zhao, X. Guo, C. Chen, C. L. Dong, R. S. Liu, C. P. Han, Y. Li, Y. Gogotsi, G. Wang, Nat. Catal. 2018, 1, 985.
- [26] a) M. Andersen, Nat. Catal. 2023, 6, 460; b) H. Xin, A. Vojvodic, J. Voss, J. K. Nørskov, F. Abild-Pedersen, Phys. Rev. B. 2014, 89, 115114.
- [27] a) S. Dupré-Crochet, M. Erard, O. Nüβe, J. Leukoc. Biol. 2013, 94,
   657; b) J. M. Robinson, Histochem. Cell Biol. 2008, 130, 281; c) U.
   Förstermann, N. Xia, H. Li, Circ. Res. 2017, 120, 713.
- [28] a) J. Zhou, W. Liu, X. Zhao, Y. Xian, W. Wu, X. Zhang, N. Zhao, F. J. Xu, C. Wang, Adv. Sci. 2021, 8, 2100505; b) Y. Ma, Q. Wang, S. Du, J. Luo, X. Sun, B. Jia, J. Ge, J. Dong, S. Jiang, Z. Li, ACS Nano 2024, 18, 5418.
- [29] I. Tabas, K. E. Bornfeldt, Circ. Res. 2016, 118, 653.
- [30] P. Libby, A. H. Lichtman, G. K. Hansson, Immunity 2013, 38, 1092.
- [31] a) M. Rath, I. Müller, P. Kropf, E. I. Closs, M. Munder, Front. Immunol. 2014, 5, 532; b) P. J. Murray, T. A. Wynn, J. Leukoc. Biol. 2011, 89, 557.
- [32] a) C. Lawson, S. Wolf, Pharmacol. Rep. 2009, 61, 22; b) M. J. Davies, J. Gordon, A. Gearing, R. Pigott, N. Woolf, D. Katz, A. Kyriakopoulos, J. Pathol. 1993, 171, 223; c) S.-J. Hwang, C. M. Ballantyne, A. R. Sharrett, L. C. Smith, C. E. Davis, A. M. Gotto Jr, E. Boerwinkle, Circulation 1997, 96, 4219.
- [33] a) C. A. Cuff, D. Kothapalli, I. Azonobi, S. Chun, Y. Zhang, R. Belkin, C. Yeh, A. Secreto, R. K. Assoian, D. J. Rader, J. Clin. Invest. 2001, 108, 1031; b) R. C. Savani, G. Cao, P. M. Pooler, A. Zaman, Z. Zhou, H. M. DeLisser, J. Biol. Chem. 2001, 276, 36770.
- [34] M. D. Rekhter, Cardiovasc. Res. 1999, 41, 376.
- [35] G. L. Basatemur, H. F. Jørgensen, M. C. Clarke, M. R. Bennett, Z. Mallat, Nat. Rev. Cardiol. 2019, 16, 727.
- [36] J. F. Bentzon, F. Otsuka, R. Virmani, E. Falk, Circ. Res. 2014, 114, 1852.
- [37] a) G. K. Hansson, P. Libby, Nat. Rev. Immunol. 2006, 6, 508; b) P. Libby, P. M. Ridker, A. Maseri, Circulation 2002, 105, 1135.
- [38] a) D. J. Tyrrell, D. R. Goldstein, Nat. Rev. Cardiol. 2021, 18, 58; b) H. Schuett, M. Luchtefeld, C. Grothusen, K. Grote, B. Schieffer, Thromb. Haemost. 2009, 102, 215.
- [39] a) A. Zernecke, E. Shagdarsuren, C. Weber, Arterioscler. Thromb. Vasc. Biol. 2008, 28, 1897; b) C. Arnaud, P. C. Beguin, S. Lantuejoul, J.-L. Pepin, C. Guillermet, G. Pelli, F. Burger, V. Buatois, C. Ribuot, J.-P. Baguet, Am. J. Respir. Crit. Care Med. 2011, 184, 724.
- [40] a) S. Collot-Teixeira, J. Martin, C. McDermott-Roe, R. Poston, J. L. McGregor, Cardiovasc. Res. 2007, 75, 468; b) K. Tian, Y. Xu, A. Sahebkar, S. Xu, Curr. Atheroscler. Rep. 2020, 22, 59; c) T. Goyal, S. Mitra, M. Khaidakov, X. Wang, S. Singla, Z. Ding, S. Liu, J. L. Mehta, Curr. Atheroscler. Rep. 2012, 14, 150.

- [41] a) R. R. Singaraja, L. R. Brunham, H. Visscher, J. J. Kastelein, M. R. Hayden, Arterioscler. Thromb. Vasc. Biol. 2003, 23, 1322; b) C. Albrecht, S. Soumian, J. Amey, A. Sardini, C. Higgins, A. Davies, R. Gibbs, Stroke 2004, 35, 2801; c) L. R. Brunham, R. R. Singaraja, M. Duong, J. M. Timmins, C. Fievet, N. Bissada, M. H. Kang, A. Samra, J.-C. Fruchart, B. McManus, Arterioscler. Thromb. Vasc. Biol. 2009, 29, 548.
- [42] a) S. Chang, G. Zhang, L. Li, H. Li, X. Jin, Y. Wang, B. Li, Atherosclerosis 2023, 373, 29; b) Y. Yan, M. Thakur, E. P. van der Vorst, C. Weber, Y. Döring, Atherosclerosis 2021, 330, 95.
- [43] P. N. Hopkins, Physiol. Rev. 2013, 93, 1317.
- [44] a) Y. Zhou, H. Zhou, L. Hua, C. Hou, Q. Jia, J. Chen, S. Zhang, Y. Wang, S. He, E. Jia, Biol. Med. 2021, 171, 55; b) S. Y. Tang, J. Monslow, L. Todd, J. Lawson, E. Puré, G. A. FitzGerald, Circulation 2014, 129, 1761; c) Y. Hui, E. Ricciotti, I. Crichton, Z. Yu, D. Wang, J. Stubbe, M. Wang, E. Puré, G. A. FitzGerald, Circulation 2010, 121, 2654.
- [45] a) L. Deng, S. He, N. Guo, W. Tian, W. Zhang, L. Luo, Inflamm. Res. 2023, 72, 281; b) Y. Sun, P. Chen, B. Zhai, M. Zhang, Y. Xiang, J. Fang, S. Xu, Y. Gao, X. Chen, X. Sui, Biomed. Pharmacother. 2020, 127, 110108; c) M. E. Burleigh, V. R. Babaev, J. A. Oates, R. C. Harris, S. Gautam, D. Riendeau, L. J. Marnett, J. D. Morrow, S. Fazio, M. F. Linton, Circulation 2002, 105, 1816; d) F. Cipollone, M. L. Fazia, J. Cardiovasc. Pharmacol. 2006, 47, S26.
- [46] a) Z. Chen, S. Ishibashi, S. Perrey, J.-i. Osuga, T. Gotoda, T. Kitamine, Y. Tamura, H. Okazaki, N. Yahagi, Y. Iizuka, Arterioscler. Thromb. Vasc. Biol. 2001, 21, 372; b) L. Zhao, Z. Varghese, J. Moorhead, Y. Chen, X. Z. Ruan, Br. Med. Bull. 2018, 126, 101.
- [47] a) A. N. Seneviratne, A. Edsfeldt, J. E. Cole, C. Kassiteridi, M. Swart, I. Park, P. Green, T. Khoyratty, D. Saliba, M. E. Goddard, *Circulation* 2017, 136, 1140; b) C. Garcia-Gonzalez, C. Dieterich, G. Maroli, M. Wiesnet, A. Wietelmann, X. Li, X. Yuan, J. Graumann, K. Stellos, T. Kubin, *Circ. Res.* 2022, 131, 580.
- [48] Z. Guo, J. Hong, N. Song, M. Liang, Acc. Mater. Res. 2024, 5, 347.
- [49] a) B. Jiang, D. Duan, L. Gao, M. Zhou, K. Fan, Y. Tang, J. Xi, Y. Bi, Z. Tong, G. F. Gao, *Nat. Protoc.* 2018, *13*, 1506; b) J.-J. Zheng, F. Zhu, N. Song, F. Deng, Q. Chen, C. Chen, J. He, X. Gao, M. Liang, *Nat. Protoc.* 2024, *13*, 1506.
- [50] a) S. Ji, B. Jiang, H. Hao, Y. Chen, J. Dong, Y. Mao, Z. Zhang, R. Gao, W. Chen, R. Zhang, *Nat. Catal.* 2021, 4, 407; b) Y. Chen, P. Wang, H. Hao, J. Hong, H. Li, S. Ji, A. Li, R. Gao, J. Dong, X. Han, *J. Am. Chem. Soc.* 2021, 143, 18643.
- [51] R. Han, Y. Xiao, Q. Bai, C. H. J. Choi, Acta Pharm. Sin. B. 2023, 13, 1847.
- [52] C. W. Dunnett, J. Am. Stat. Assoc. 1955, 50, 1096.